

## NATURAL HAZARDS

# The complex dynamics of the 2023 Kahramanmaraş, Turkey, $M_w$ 7.8-7.7 earthquake doublet

Zhe Jia<sup>1\*</sup>, Zeyu Jin<sup>1</sup>, Mathilde Marchandon<sup>2</sup>, Thomas Ulrich<sup>2</sup>, Alice-Agnes Gabriel<sup>1,2</sup>, Wenyuan Fan<sup>1</sup>, Peter Shearer<sup>1</sup>, Xiaoyu Zou<sup>1</sup>, John Rekoske<sup>1</sup>, Fatih Bulut<sup>3</sup>, Asli Garagon<sup>3</sup>, Yuri Fialko<sup>1</sup>

The destructive 2023 moment magnitude ( $M_w$ ) 7.8-7.7 earthquake doublet ruptured multiple segments of the East Anatolian Fault system in Turkey. We integrated multiscale seismic and space-geodetic observations with multifault kinematic inversions and dynamic rupture modeling to unravel the events' complex rupture history and stress-mediated fault interactions. Our analysis reveals three subshear slip episodes during the initial  $M_w$  7.8 earthquake with a delayed rupture initiation to the southwest. The  $M_w$  7.7 event occurred 9 hours later with a larger slip and supershear rupture on its western branch. Mechanically consistent dynamic models accounting for fault interactions can explain the unexpected rupture paths and require a heterogeneous background stress. Our results highlight the importance of combining near- and far-field observations with data-driven and physics-based models for seismic hazard assessment.

The moment magnitude ( $M_w$ ) 7.8 and 7.7 Kahramanmaraş earthquakes in Turkey on 6 February 2023 caused enormous destruction and tens of thousands of casualties from collapsed structures and together were one of the deadliest natural disasters for Turkey and Syria over the past millennium (1). The Kahramanmaraş sequence is the first great earthquake doublet with a combined moment magnitude of 8 recorded in a continental strike-slip fault system. Unlike regular aftershocks that are more than one order of magnitude smaller than their mainshock, doublet events pose a greater hazard because they can cause more severe damage by striking already weakened buildings and structures. We show that the Kahramanmaraş earthquake doublet involved a remarkable sequence of subevents that occurred with varying rupture velocities, geometries, and time delays on branched fault segments, which challenge our understanding of earthquake interactions and the dynamics of rupture propagation.

Seismologists commonly approximate earthquakes as point sources or as slip along a single fault with fixed rupture velocity. However, large earthquakes often rupture multiple fault segments within a complex network (2–6). Occasionally, events of a comparable magnitude occur within minutes to hours of the initial event, resulting in earthquake doublets (7–9). Branching faults may further complicate rupture dynamics (10–12). Whether rupture stops or continues propagating at fault junctions can determine earthquakes' eventual size and destructive potential (13). When

applied to complex ruptures on multiple faults, conventional earthquake source imaging often involves oversimplified assumptions, yielding stark differences in source models and their interpretations (14, 15). Initial studies of the Kahramanmaraş earthquakes presented a wide range of earthquake models and interpretations (16–21), likely from focusing on particular datasets and aspects of the rupture process. These differences motivate unified and self-consistent approaches that integrate diverse datasets with state-of-the-art rupture models to advance our understanding of the earthquake dynamics.

We performed a comprehensive investigation of the  $M_w$  7.8-7.7 Kahramanmaraş doublet using data-driven and physics-based analyses applied to near- and far-field seismic and geodetic observations. Our results reveal that the earthquakes followed unexpected rupture trajectories, which included delayed backward branching, statically and dynamically aided triggering, and a combination of subshear and supershear rupture episodes. These discoveries call for reevaluating the role of cascading failure mechanisms when assessing the destructive potential of large earthquakes within complex fault networks.

## The geometrically complex $M_w$ 7.8-7.7 earthquake doublet

On 6 February 2023, two major ( $M_w > 7$ ) earthquakes ruptured several previously recognized fault systems within 9 hours (Fig. 1). The East Anatolian Fault (EAF) is a mature transform fault accommodating up to 10 mm/year of left-lateral motion between the Arabian and Anatolian plates (Fig. 1) (22). Several  $M_w \sim 7$  earthquakes occurred on the EAF historically, but none ruptured the entire southern section of the EAF (23). The estimated dimensions of the historic events suggest that geometric complexities such as fault bends and step-overs may have controlled the event sizes (23, 24).

The second earthquake ( $M_w$  7.7) occurred on the Savrun-Çardak Fault (SCF), extending  $\sim 150$  km along the east-west direction (Fig. 1). The SCF has been relatively quiescent, with only two moderate ( $M_w < 6$ ) events recorded in the past 100 years (25).

We constrained the rupture geometry on the basis of surface traces mapped using Synthetic Aperture Radar data (26) and precisely relocated aftershocks (27, 28). We found that the Kahramanmaraş doublet ruptured at least six major fault segments (Fig. 1). The epicenter of the  $M_w$  7.8 earthquake is located on a subsidiary fault, the Nurdağı-Pazarcık (Narlı) Fault (NPF) (Fig. 1A, fault 1) (20), from which the rupture propagated to the EAF, and then ruptured along the EAF to both the northeast and southwest (Fig. 1A, faults 2 and 3), for a total length of about 300 km. Unlike the historical  $M_w \sim 7$  events, the  $M_w$  7.8 earthquake propagated across at least four possible geometric barriers, including fault bends and stepovers.

The static slip distribution (Fig. 1B) obtained from inversions of Synthetic Aperture Radar (SAR) and Global Navigation Satellite System (GNSS) data (figs. S1 to S7) shows that the largest slip in the  $M_w$  7.8 event is on the EAF at its junction with the NPF, near the towns of Kahramanmaraş and Pazarcık, with a peak slip in excess of 8 m. Most of the coseismic slip is in the upper 20 km of the seismogenic layer (Fig. 1B). Slip at the surface is highly heterogeneous, which is consistent with field observations (18), but on average increases from the southwest to the northeast ends of the  $M_w$  7.8 rupture (fig. S8). The area of substantial slip extends to the northeast from the junction for about 150 km to the western tip of the 2020  $M_w$  6.7 Elazığ rupture (Fig. 1A) (29). South of the junction, the  $M_w$  7.8 rupture extends to the southern end of the EAF. The average coseismic slip on the southwest branch of the  $M_w$  7.8 rupture is smaller than the average slip on the northeast branch (Fig. 1B and fig. S2).

We resolved the spatiotemporal rupture process with a subevent inversion method by using both near- and far-field seismic observations (30, 31). The  $M_w$  7.8 earthquake had six subevents that altogether spanned  $\sim 90$  s (Fig. 2A). The  $M_w$  6.8 subevent E1 that ruptured the NPF was followed 18 s later by the largest subevent E2 ( $M_w$  7.5) at the NPF-EAF intersection. The earthquake then ruptured northeastward along the EAF for about 130 km ( $M_w$  7.5 subevent E3), as well as, after a short delay, backward from the NPF junction for about 150 km along the southwestern segment of the EAF, with an integrated slip equivalent to a  $M_w$  7.4 earthquake (subevents E4 to E6). Teleseismic  $P$  wave back-projection (32) confirmed the rupture process, with imaged high-frequency radiation peaks outlining the major subevents (Fig. 2A) and indicating an average



<sup>1</sup>Scripps Institution of Oceanography, University of California, San Diego, La Jolla, CA 92093, USA. <sup>2</sup>Department of Earth and Environmental Sciences, Ludwig-Maximilians-Universität München, 80539 Munich, Germany. <sup>3</sup>Geodesy Department, Bogazici University Kandilli Observatory and Earthquake Research Institute, Istanbul 34342, Turkey.  
\*Corresponding author. Email: z5jia@ucsd.edu

rupture velocity of 3 km/s. To further constrain the slip history, we performed a joint kinematic slip inversion of the  $M_w$  7.8 earthquake constrained by far- and near-field seismic and geodetic data (26, 33). Our kinematic

inversion results agree with the static and subevent models (Fig. 2B). The best-fit kinematic slip model images 10-s-delayed backward branching at the NPF-EAF intersection, toward the southwest (Fig. 2B), constrained by the

strong-motion data (fig. S17). It also indicates average rupture velocities of 3.2 km/s and 2.8 km/s for the northeastern and southwestern branches, respectively (fig. S18). Tracking ground motion pulses at near-fault strong

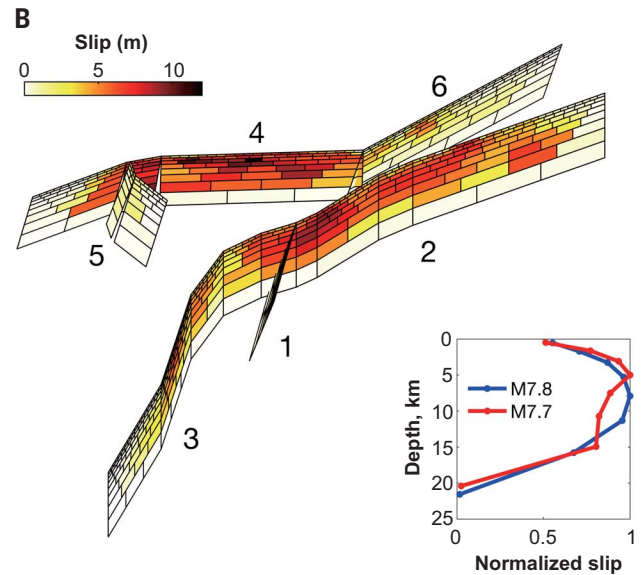
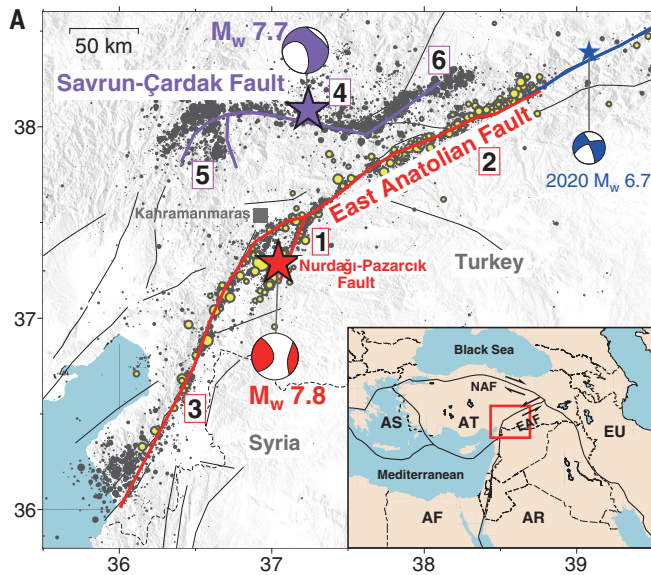


**Fig. 1. A multifault earthquake doublet.** (A) Tectonic background and aftershock seismicity of the study area near Kahramanmaraş, Turkey. Red and purple stars indicate the  $M_w$  7.8 and 7.7 earthquake epicenters according to the Turkey Disaster and Emergency Management Authority (53), and red and purple beachballs indicate focal mechanisms from the Global Centroid Moment Tensor catalog, respectively. Red and purple lines indicate surface ruptures identified from SAR data (26). Yellow dots indicate aftershocks for the period between the  $M_w$  7.8 and 7.7 earthquakes, and black dots indicate aftershocks after the  $M_w$  7.7 event (28). The blue line and

blue beachball denote the rupture extent and focal mechanism of the 2020  $M_w$  6.7 Elazığ earthquake (29). (Inset) The regional tectonics and major plate boundary faults (solid black lines). Red outline denotes the study area. (B) Finite-fault model of the 2023 doublet derived from inversions of space geodetic (InSAR and GNSS) data. Fault segment numbers correspond to those shown in (A), in order of their rupture time: 1, Nurdagi-Pazarcik Fault; 2 and 3; East Anatolian Fault; 4 to 6, Savrun-Çardak Fault. (Inset) The along-strike averaged coseismic slip normalized by the maximum slip amplitude, as a function of depth (49).

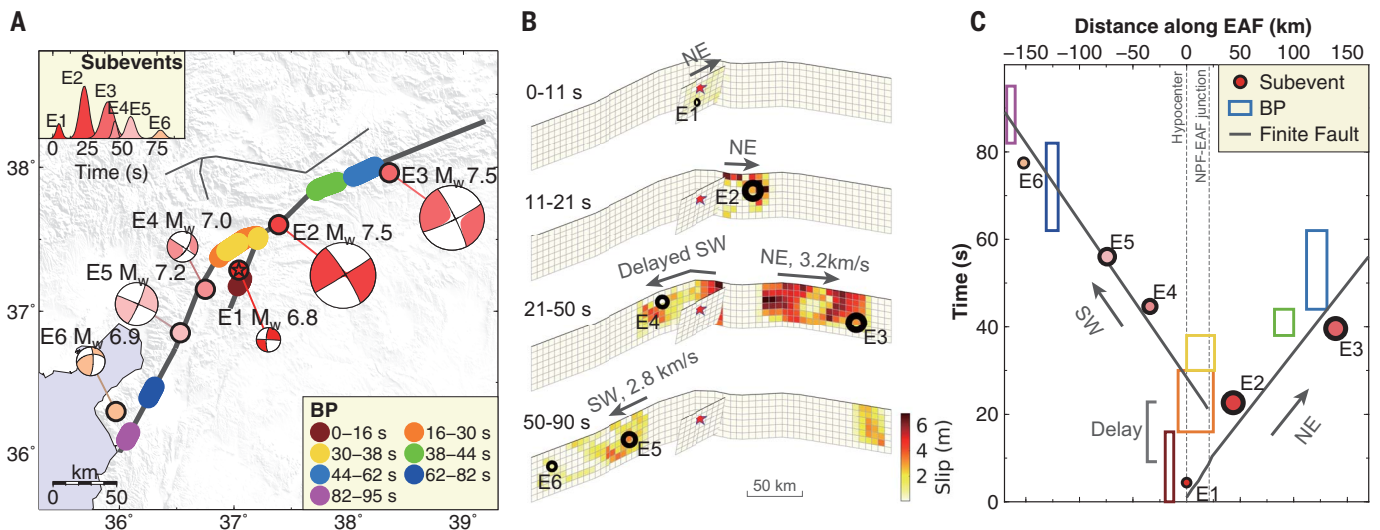


**Fig. 2. Complex slip evolution of the  $M_w$  7.8 earthquake, including delayed initiation of slip.** (A) Subevent model from near- and far-field seismic observations and back-projection results, suggesting that the  $M_w$  7.8 earthquake initiated on the NPF-1 (Fig. 1B, fault 1), then propagated bilaterally, northeast along the EAF-2 (Fig. 1B, fault 2) and southwest along the EAF-3 (Fig. 1B, fault 3). The rupture of fault 2 terminates around 50 s, whereas rupture of fault 3 continues for an additional 30 s. (B) Rupture history within different time

intervals from our kinematic slip inversion of far- and near-field seismic and geodetic data. We infer rupture velocities of 3.2 and 2.8 km/s for the northeast and southwest episodes, respectively, and a 10-s delay in the onset of the southwest rupture along EAF-3 with respect to the NE rupture along EAF-2. The slip distribution within each time interval agrees with the subevent (black circles) inversion. (C) Subevents, back-projection locations and times, and finite-fault velocities [in (B)] consistently indicate delayed initiation of slip on branch EAF-3.

motion stations along the southwestern segment also yielded a rupture velocity of  $\sim 3$  km/s (fig. S18), confirming an overall subshear nature. All our kinematic models consistently reveal a  $\sim 300$ -km-long complex bilateral multisegment rupture, subshear rupture velocities, and delayed triggering of the southwest segment of the  $M_w$  7.8 event (Fig. 2C).

The subsequent  $M_w$  7.7 earthquake ruptured a 150-km-long section of the west-trending SCF, within 90 km of the  $M_w$  7.8 earthquake hypocenter. The aftershock distribution and surface offsets indicate branching and abrupt changes in strike at both the eastern and western ends of the  $M_w$  7.7 rupture (Fig. 1). Geodetic data and our associated static slip model (Fig. 1B) suggest rupture along an 80-km-long segment of the SCF system (Fig. 1, faults 4 and 5), but not along the eastern end of the Sürgü fault that connects to the EAF. Instead, the  $M_w$  7.7 rupture diverted sharply onto the Doğanşehir branch, which angles to the northeast (Fig. 1, fault 6). The  $M_w$  7.7 event shows a concentrated slip distribution with  $>10$  m peak slip around its hypocenter, suggesting a substantially higher stress drop than that of the initial  $M_w$  7.8 earthquake, which spread a lower-amplitude slip over a larger region.

Our analysis of the rupture history of the  $M_w$  7.7 event identified four major subevents, lasting for about 30 s (Fig. 3A). The first three subevents, E1 to E3, all cluster near the epicenter and account for more than 80% of the total seismic moment, suggesting a compact

bilateral rupture in the central SCF. The focal mechanism (strike of  $237^\circ$ ) and location of the last subevent (E4;  $M_w$  7.1) agree with the static slip model on the Doğanşehir branch (Fig. 1B). All subevents of both earthquakes have almost pure double-couple mechanisms (Figs. 2A and 3A), suggesting that the strong non-double-couple components in the Global Centroid-Moment-Tensor solutions (Fig. 1A) (34) are due to highly variable rupture geometries. The overall shorter duration and smaller rupture extent of the  $M_w$  7.7 event make back-projection analysis less effective for resolving rupture details, but our kinematic finite-slip inversion can still be applied.

The kinematic finite-fault model of the  $M_w$  7.7 earthquake also indicates a compact slip distribution. In addition, it indicates a westward rupture velocity of  $\sim 4.5$  km/s (Fig. 3B), exceeding the shear-wave speed in the crust. The waveforms recorded at the westward seismic stations strongly constrain this supershear rupture episode (Fig. 3C and fig. S19), which is consistent with analysis of high-rate GNSS data (20). By contrast, the eastward rupture likely propagated at a slower velocity of 2.5 km/s. The intriguing supershear rupture episode may imply locally higher prestress (35) and high stress drop (36) as in our dynamic rupture models.

### Dynamics, triggering, and stress interaction of the doublet

Dynamic rupture modeling involves simulating how earthquakes nucleate, propagate, and

arrest. Unlike purely data-driven kinematic slip inversions, such models predict the evolution of slip, seismic waves, and surface deformation in a physically self-consistent manner. Detailed, physics-based interpretations can help verify whether inferred rupture scenarios are mechanically plausible but are computationally challenging and typically take years to develop [for example, (10, 12, 13)].

We present data-informed dynamic rupture simulations of the 2023 Kahramanmaraş earthquakes that illuminate complex details of the rupture process. Our three-dimensional (3D) dynamic rupture models include stress changes computed from the slip distribution of the static slip model (37), large-scale variability in fault loading inferred from regional seismotectonics, and the relative effects of the static and dynamic stresses of the  $M_w$  7.8 event on the faults hosting the second earthquake (fig. S20) (26). The dynamic rupture models independently reproduce the main features of the kinematic models (Fig. 4 and fig. S21), providing a physics-based validation of the inferred rupture histories.

Our forward simulations use the complex fault geometries of both earthquakes informed from geodetic analysis (Fig. 1) to spontaneously replicate the moment rate release, magnitude, rupture velocity and delays, as well as the lack of instantaneous dynamic triggering of the  $M_w$  7.7 event. The dynamic rupture synthetics produce surface displacements and slip histories that compare well with the high-resolution geodetic data (fig. S22), kinematic rupture

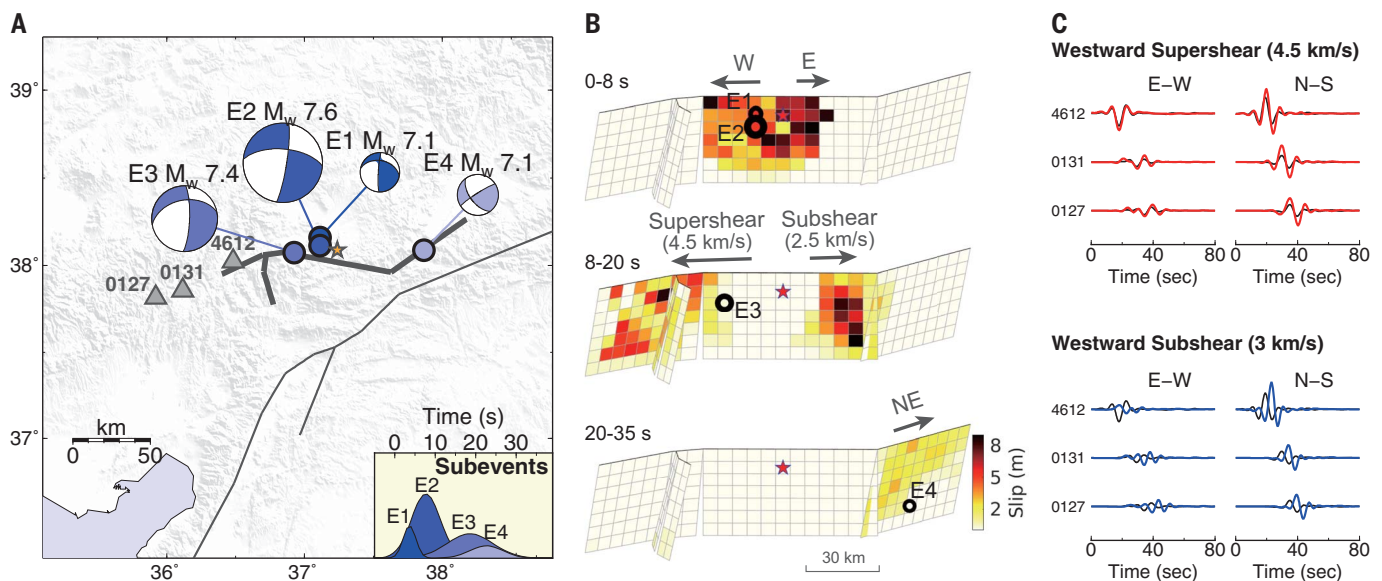


**Fig. 3. Asymmetric kinematics of the  $M_w$  7.7 earthquake.** (A) Three subevents close to the hypocenter suggest a bilateral rupture. The fourth event images the rupture of the Doğanşehir branch (Fig. 1B, fault 6). (B) Asymmetric bilateral rupture velocities of the  $M_w$  7.7 event. The westward rupture has an inferred supershear velocity of 4.5 km/s, whereas a subshear velocity is seen toward the east (2.5 km/s). Subevent locations are based on their seismic moment

centroids. The slip may not be the largest at the centroid location, specifically for bilateral ruptures. For example, E3 (10 to 30 s) averages slip pulses of both the westward supershear and the eastward subshear rupture. (C) A westward supershear rupture velocity (red waveforms) better explains observed waveforms (black) at near-fault strong motion stations to the west [triangles in (A)] than a subshear rupture (blue).

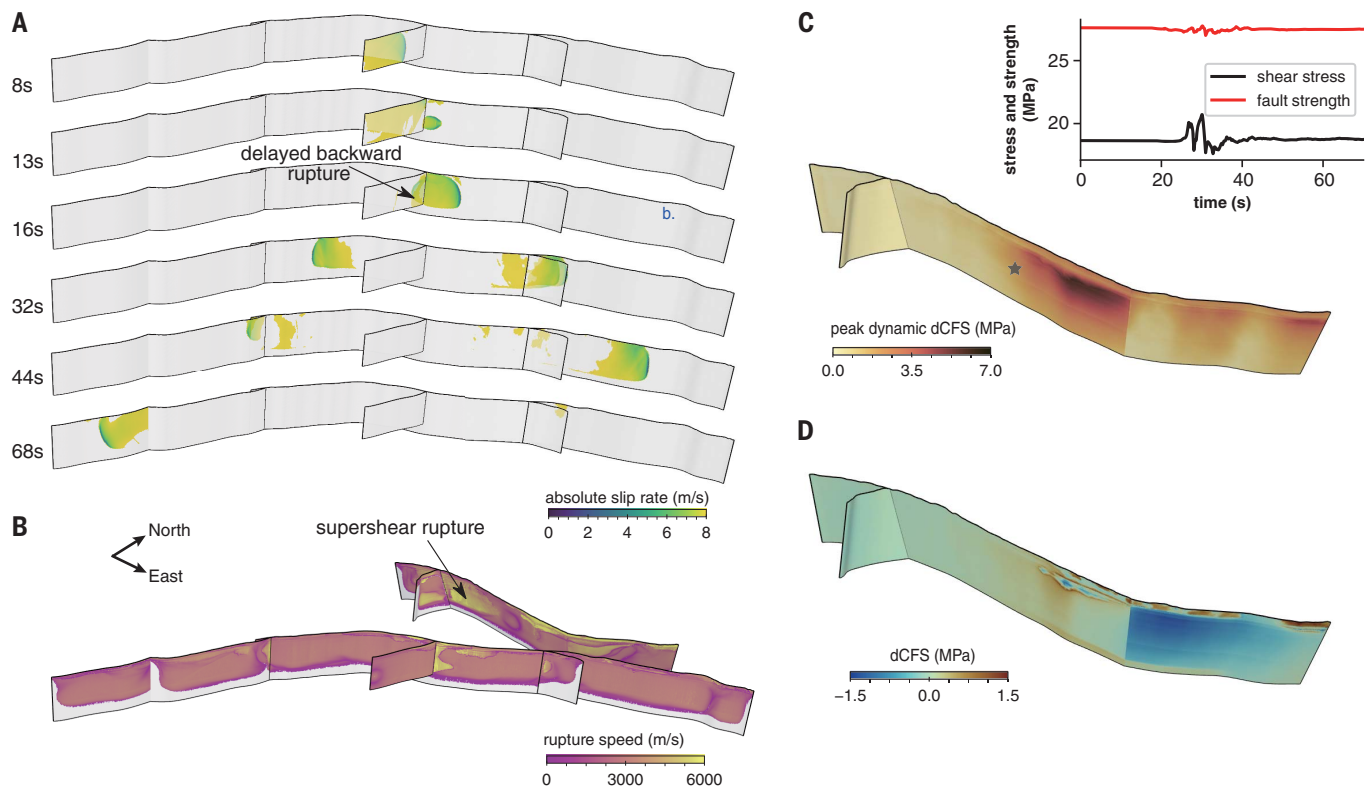


**Fig. 4. 3D dynamic rupture scenarios and stress-mediated interactions of the  $M_w$  7.8 and 7.7 earthquakes.** (A) Snapshots of absolute slip rate evolution in the  $M_w$  7.8 dynamic rupture scenario (movie S1). (B) Modeled rupture speeds in linked dynamic rupture simulations (54) of both earthquakes indicating dominantly subshear rupture speeds but sustained westward supershear during the  $M_w$  7.7

scenario (fig. S21 and movie S2). (C) Peak absolute dynamic shear stress perturbation reaching up to 7 MPa measured in the direction of maximum initial traction. (Inset) Evolution of dynamic shear stress and fault strength at the  $M_w$  7.7 hypocenter (black star). (D) Static Coulomb failure stress changes ( $\Delta CFS$ ) assuming a static friction coefficient of 0.6.

representations (Fig. 4 and fig. S21), and observed ground motions (Fig. 5 and figs. S23 to S25). The modeled  $M_w$  7.8 earthquake dynamics are illustrated in Fig. 4A. The NPF-EAF intersection slows subshear rupture on the NPF that then branches with dynamically favorable forward directivity (38) northeastward along the EAF. The large fault branching angle poses a strong dynamic barrier in backward-directivity (39), leading to substantially delayed EAF rupture toward the southwest. Continuous dynamic unclamping, transient shear stressing, and static stress buildup at the fault intersection due to the unilaterally propagating northeast rupture allowed the rupture to eventually fracture the EAF bilaterally (fig. S26). Rupture speed remained overall subshear during the earthquake (Fig. 4B).

Dynamic rupture modeling of the  $M_w$  7.7 earthquake features bilateral rupture with unequal rupture speeds, confirming dominant supershear westward and subshear eastward propagation. Our  $M_w$  7.8 dynamic rupture model predicts a highly variable pattern of static and dynamic stresses resolved on the faults that hosted the  $M_w$  7.7

event experienced an increase in static Coulomb stress of several hundred kilopascals because of the  $M_w$  7.8 earthquake, resulting from both an increase in shear stress and a decrease in fault-normal compression (fig. S27). It also experienced a much larger transient increase in the Coulomb stress of a few megapascals owing to passing seismic waves (Fig. 4C), which nevertheless did not result in instantaneous triggering.

#### Discussion and conclusions

Our analyses reveal unexpected rupture paths. The Kahramanmaraş doublet originated as a moderate event on the NPF branch fault with a magnitude of only 6.8, yet the rupture was able to successfully cross the junction of the NPF and EAF, which would usually be considered a geometric barrier that conditionally gates the rupture propagation (40, 41). As a result, the earthquake intensified with the northeastward propagation along the EAF then dynamically triggered backward rupture toward the southwest by continuously unclamping and stressing from the forward branch, eventually culminating in a  $M_w$  7.8 event, with total seismic moment increased by a factor of 30 com-

pared with the initial rupture on the NPF. In addition, the  $M_w$  7.8 earthquake increased the Coulomb stress on the central part of the SCF, which may have aided the nucleation of the  $M_w$  7.7 earthquake 9 hours later. The entire process highlights the additional hazard brought by rupture triggering across a network of faults, challenging earthquake hazard assessments that typically do not consider such multifault-triggering scenarios.

The  $M_w$  7.8 earthquake involved backward fault branching, which is highly unfavorable from a dynamic perspective, thus commonly neglected in hazard studies. Several previous continental earthquakes—including the 1992 Landers, the 1999 Hector Mine, and the 2002 Denali earthquakes—have also exhibited localized backward branching (10). Existing explanations of this phenomenon include backward rupture jumping induced by sudden rupture arresting or nonuniform prestress fields caused by earthquake cycles (39, 42). Our dynamic rupture models indicate that backward branching during the  $M_w$  7.8 event does not necessarily require a complex arrangement of the receiver fault (42) or triggering of supershear rupture (43). Instead, the progressive build-up of slip on

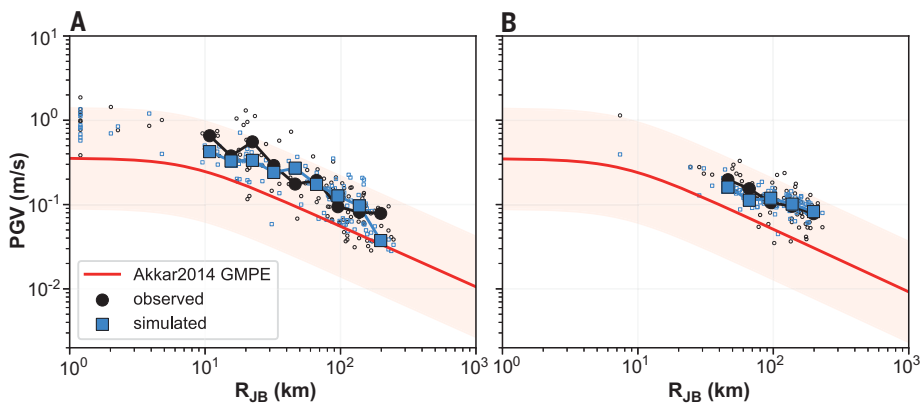


**Fig. 5. Peak ground velocities (PGVs) plotted against Joyner-Boore distance ( $R_{JB}$ ) for the  $M_w$  7.8 and  $M_w$  7.7 earthquakes.** (A) The  $M_w$  7.8 earthquake. (B) The  $M_w$  7.7 earthquake. Observed PGVs from strong motion accelerometers are indicated with open black circles, and simulated PGVs from the dynamic rupture simulations are indicated with open blue squares. We bin the PGV data by  $R_{JB}$  and plot the medians for each distance bin (solid markers). The red curve indicates PGV predicted by a ground motion model (55), assuming an average shear wave velocity for the top 30 m of soil ( $VS_{30}$ ) of 760 m/s, with the shaded area denoting its uncertainty. All PGV are rotationally independent geometric mean values (GMRotD50). We include simulated and observed data at the same locations, respectively.

the forward branch of the EAF continuously unclamps and stresses the backward branch of the EAF, eventually leading to a delayed and self-sustained branching toward the southwest, which is a simple yet effective mechanism.

One of the unexpected aspects of the  $M_w$  7.7 earthquake is that it did not rupture through the eastern Sürgü segment and arrive at the EAF, contrary to earlier suggestions (20), but instead deviated to the Doğanşehir branch. The Interferometric Synthetic Aperture Radar (InSAR), aftershock, and seismic data clearly show such a deviation (figs. S1 and S14). The straightforward rupture path along the Sürgü fault was encouraged by the static stress changes from the  $M_w$  7.8 event (fig. S27), unlike the sharp deviation to the Doğanşehir fault, which was actually unloaded by the  $M_w$  7.8 event (Fig. 4D and movie S3). Possible explanations, which may be tested by future geodetic and seismological observations, include velocity-strengthening behavior of the eastern Sürgü segment or local stress heterogeneity, for example, because of past earthquakes (44). Considerable regional stress heterogeneity, as is required by our dynamic rupture models (fig. S20), is implied by extremely complex rupture geometries that involve changes in the strike angle of up to  $90^\circ$  (Fig. 1 and fig. S27) (45). Some faults in the study area, including the EAF, exhibit shallow creep (46); however, creep has to be pervasive to potentially suppress an incoming dynamic rupture. Observations spanning all phases of the earthquake cycle are needed to constrain the velocity- and depth-dependent frictional properties of active faults (47, 48). Shallow creep might be responsible for a substantial reduction in the amplitude of coseismic slip in the top few kilometers of the upper crust (Fig.

1B), which is well resolved in our inverse models (fig. S28). Subsequent observations will show whether this reduction can be compensated by shallow afterslip or constitutes a long-term shallow slip deficit (49), implying widespread off-fault yielding (47, 50).

We also found intriguing variations in rupture velocity across segments of the EAF-SCF fault network. Although the  $M_w$  7.8 event produced extreme shaking with peak ground accelerations (PGAs) exceeding 1 g for near-fault stations, the observed and simulated  $M_w$  7.7 ground motions are similar or larger when compared at the same distance (Fig. 5 and figs. S23 and S24), which is consistent with a potentially larger stress drop of the  $M_w$  7.7 event. The modeled and observed  $M_w$  7.7 event shaking shows less distance dependence, which may be due to the effects of supershear rupture.

The western branch of the SCF experienced a supershear rupture episode, whereas the eastern SCF branch and the EAF hosted subshear ruptures with considerable delays. In general, our modeling shows that the pre-event stress heterogeneities, dynamic and static redistribution of stress, and the geometry of the faults may control these diverse rupture characteristics.

The Kahramanmaraş doublet ruptured multiple faults in distinct slip episodes, likely involving complex stress-triggering processes across different temporal and spatial scales. Such processes resulted in the increased rupture length and seismic moment of the Turkey earthquake doublet, and a substantially larger destructive potential compared with the “typical”  $M_w \sim 7$  historical earthquakes in the region (23). Such a variability might be interpreted in terms of the supercycle model (51). By using integrated methods that combine near- and far-

field seismic and geodetic observations and investigating data-derived models and physics-based rupture simulations, we show that stress interactions and static and dynamic triggering worked together across a complex fault system, resulting in a cascade of rupture with a larger than usual total rupture length and moment magnitude. Our study shows that complementary data-driven and physics-based analyses, which in isolation often lead to non-unique or even contradictory results, can jointly and efficiently unravel highly complex earthquake dynamics based on dense near-field observations. The unusual static and dynamic interactions during and between the events of the Kahramanmaraş doublet call for reassessment of common assumptions built into seismic hazard assessments.

## REFERENCES AND NOTES

- M. Edrik, M. B. D. Tümsa, A. Pınar, E. Altunel, A. C. Zülfiakar, “A preliminary report on the February 6, 2023 earthquakes in Türkiye” (Temblok, 2023).
- T. Lay, L. Ye, Y. Bai, K. F. Cheung, H. Kanamori, *Geophys. Res. Lett.* **45**, 9542–9551 (2018).
- L. Meng *et al.*, *Science* **337**, 724–726 (2012).
- E. Hauksson, L. M. Jones, K. Hutton, *Bull. Seismol. Soc. Am.* **92**, 1154–1170 (2002).
- E. Hauksson, L. M. Jones, K. Hutton, D. Eberhart-Phillips, *J. Geophys. Res.* **98** (B11), 19835–19858 (1993).
- Z. E. Ross *et al.*, *Science* **366**, 346–351 (2019).
- A. Ghods *et al.*, *Geophys. J. Int.* **203**, 522–540 (2015).
- C. J. Ammon, H. Kanamori, T. Lay, *Nature* **451**, 561–565 (2008).
- W. Fan, P. M. Shearer, *Science* **353**, 1133–1136 (2016).
- D. D. Oglesby, S. M. Day, Y.-G. Li, J. E. Vidale, *Bull. Seismol. Soc. Am.* **93**, 2459–2476 (2003).
- H. S. Bhat, M. Olives, R. Dmowska, J. R. Rice, *J. Geophys. Res.* **112** (B11), B11309 (2007).
- T. Ulrich, A.-A. Gabriel, J.-P. Ampuero, W. Xu, *Nat. Commun.* **10**, 1213 (2019).
- R. Douilly, H. Aochi, E. Calais, A. Freed, *J. Geophys. Res. Solid Earth* **120**, 1108–1128 (2015).
- S. Minson, M. Simons, J. Beck, *Geophys. J. Int.* **194**, 1701–1726 (2013).
- K. Wang, D. S. Dreger, E. Tinti, R. Bürgmann, T. Taira, *Bull. Seismol. Soc. Am.* **110**, 1603–1626 (2020).
- S. Barbot *et al.*, *Seismica* 10.26443/seismica.v2i3.502 (2023).
- D. E. Goldberg *et al.*, *Seismic Record* **3**, 156–167 (2023).
- V. Karabacak *et al.*, *J. Geol. Soc. London* **180**, jgs2023–jgs2020 (2023).
- P. M. Mai *et al.*, *Seismic Record* **3**, 105–115 (2023).
- D. Melgar *et al.*, *Seismica* 10.26443/seismica.v2i3.387 (2023).
- R. Okuwaki, Y. Yagi, T. Taymaz, S. P. Hicks, *Geophys. Res. Lett.* **50**, e2023GL103480 (2023).
- N. Lyberis, T. Yurur, J. Chorowicz, E. Kasapoglu, N. Gundogdu, *Tectonophysics* **204**, 1–15 (1992).
- S. E. Güvercin, H. Karabulut, A. Ö. Konca, U. Doğan, S. Ergintav, *Geophys. J. Int.* **230**, 50–69 (2022).
- T. Y. Duman, Ö. Emre, *Spec. Publ. Geol. Soc. Lond.* **372**, 495–529 (2013).
- A. Koç, N. Kaymakci, *J. Geodyn.* **65**, 292–307 (2013).
- Materials and methods are available as supplementary materials.
- Z. Jin, Y. Fialko, *Bull. Seismol. Soc. Am.* **110**, 1660–1679 (2020).
- A. Lomax, Precise, NLL-SSST-coherence hypocenter catalog for the 2023  $M_w$  7.8 and  $M_w$  7.6 SE Turkey earthquake sequence. *Zenodo* (2023); <https://doi.org/10.5281/zenodo.8089273>.
- A. Doğru, F. Bulut, C. Yaltrak, B. Aktuğ, *Geophys. J. Int.* **224**, 389–400 (2021).
- Z. Jia *et al.*, *Earth Planet. Sci. Lett.* **531**, 115997 (2020).
- Z. Jia, Z. Zhan, H. Kanamori, *Geophys. Res. Lett.* **49**, e2021GL097104 (2022).
- M. Ishii, P. M. Shearer, H. Houston, J. E. Vidale, *Nature* **435**, 933–936 (2005).
- Z. Jia, X. Wang, Z. Zhan, *Geophys. Res. Lett.* **47**, e2020GL089802 (2020).
- G. Ekström, M. Nettles, A. Dziewowski, *Phys. Earth Planet. Inter.* **200–201**, 1–9 (2012).

35. C. Liang, J. P. Ampuero, D. Pino Muñoz, *Geophys. Res. Lett.* **49**, e2022GL099749 (2022).
36. E. M. Dunham, *J. Geophys. Res. Solid Earth* **112**, JB004717 (2007).
37. E. Tinti *et al.*, *Earth Planet. Sci. Lett.* **576**, 117237 (2021).
38. N. Kame, J. R. Rice, R. Dmowska, *J. Geophys. Res. Solid Earth* **108**, JB002189 (2003).
39. S. Fliss, H. S. Bhat, R. Dmowska, J. R. Rice, *J. Geophys. Res. Solid Earth* **110**, JB003368 (2005).
40. G. King, J. Nabecaronlek, *Science* **228**, 984–987 (1985).
41. D. Andrews, *J. Geophys. Res.* **94**, 9389–9397 (1989).
42. B. Duan, D. D. Oglesby, *J. Geophys. Res. Solid Earth* **112**, JB004443 (2007).
43. A. Rosakis, M. Abdelmeguid, A. Elbanna, Evidence of early supershear transition in the  $M_w$  7.8 Karamanmaraş earthquake from near-field records. arXiv:2302.07214 [physics.geo-ph] (2023).
44. S. S. Nalbant, J. McCloskey, S. Steacy, A. A. Barka, *Earth Planet. Sci. Lett.* **195**, 291–298 (2002).
45. Y. Fialko, *J. Geophys. Res. Solid Earth* **126**, e2021JB022000 (2021).
46. Z. Cakir *et al.*, *Earth Planet. Sci. Lett.* **608**, 118085 (2023).
47. Y. Kaneko, Y. Fialko, D. T. Sandwell, X. Tong, M. Furuya, *J. Geophys. Res. Solid Earth* **118**, 316–331 (2013).
48. E. O. Lindsey, Y. Fialko, *J. Geophys. Res. Solid Earth* **121**, 1097–1113 (2016).
49. Y. Fialko, D. Sandwell, M. Simons, P. Rosen, *Nature* **435**, 295–299 (2005).
50. Z. Jin, Y. Fialko, *Geophys. Res. Lett.* **48**, e2021GL095213 (2021).
51. L. Dal Zilio, J.-P. Ampuero, *Commun. Earth Environ.* **4**, 71 (2023).
52. L. Luzzi *et al.*, *Bull. Earthquake Eng.* **18**, 5533–5551 (2020).
53. Disaster and Emergency Management Authority (AFAD) (1973); <https://deprem.afad.gov.tr/event-catalog>.
54. T. Taufiqurrahman *et al.*, *Nature* **618**, 308–315 (2023).
55. S. Akkar, M. A. Sandikkaya, J. J. Bommer, *Bull. Earthquake Eng.* **12**, 359–387 (2014).
56. Z. Jia *et al.*, 2023\_Turkey\_doublet\_Data\_Model. Zenodo (2023); <https://doi.org/10.5281/zenodo.8128343>.

## ACKNOWLEDGMENTS

We thank two anonymous reviewers for constructive comments. The facilities of IRIS Data Services, and specifically the IRIS Data Management Center, were used for access to waveforms, related metadata, and/or derived products used in this study. The GNSS data are provided by the General Directorate of Land Registry and Cadastre and the General Directorate of Mapping, Turkey. IRIS Data Services are funded through the Seismological Facilities for the Advancement of Geoscience (SAGE) Award of the National Science Foundation under Cooperative Support Agreement EAR-1851048. We thank the Engineering Strong-Motion (ESM) Database by ORFEUS (52) for providing access to the data from the Turkish National Strong Motion Network, which is operated by Turkey's Disaster and Emergency Management Authority (AFAD). The computations in this study were supported by the supercomputer SuperMUC-NG. **Funding:** Funding for this work was provided by the National Science Foundation (EAR-2123529, EAR-1841273 to Y.F., EAR-2022441, EAR-2143413 to W.F., and EAR-2121568 to A.-A.G.), the National Aeronautics and Space Administration (80NSSC22K0506 to Y.F., 80NSSC20K0495 to A.A.G.), the United States Geological Survey (G22APO0011 to P.S. and W.F.), and the Cecil and Ida Green Foundation. M.M., T.U., and A.-A.G. were supported by the European Union's Horizon 2020 Research and Innovation Programme (TEAR grant 852992) and Horizon Europe (ChEES-2P grant 101093038, DT-GEO grant 101058129, and Geo-INQUIRE grant 101058518). J.R. was supported by the National Science Foundation Graduate Research Fellowship Program (grant DGE-2038238). A.-A.G. gratefully acknowledges the Gauss Centre for Supercomputing e.V. (<https://www.gauss-centre.eu>) for providing computing time on the GCS Supercomputer SuperMUC-NG at Leibniz Supercomputing Centre (<https://www.lrz.de>), in project pr49ha. **Author contributions:** Z. Jia led the study, performed the subevent and kinematic slip inversions, and wrote the initial draft of the manuscript. Z. Jin, X.Z., and Y.F. processed the InSAR data, quantified the fault geometry, and performed static slip inversion. M.M., T.U., and A.-A.G. performed the dynamic rupture simulations and the Coulomb failure stress analysis. W.F. performed

back projection analysis and coordinated the collaboration. Y.F. conducted static Coulomb stress calculations. X.Z. contributed to the fault geometry determination and figure design. J.R., T.U., and A.-A.G. conducted the ground motion analysis. F.B. and A.G. processed the GNSS data. W.F., P.S., A.-A.G., and Y.F. supervised the modeling and contributed to interpretation of the results. A.A.G., Y.F., and W.F. provided access to computational resources. All authors discussed the results and contributed to writing and revising the manuscript. **Competing interests:** The authors declare no competing interests. **Data and materials availability:** The Sentinel-1 SAR data are provided by the European Space Agency (ESA) and mirrored at the Alaska SAR Facility (ASF). The ALOS-2 PALSAR data are owned by the Japanese Space Agency (JAXA) and provided to Y.F. under a Research User Agreement. The global seismic data are publicly available from the IRIS-DMC. The regional strong motion data are publicly available from the EMS Database by ORFEUS. The geodetic and seismic data, the data-driven slip models and subevent models, and the data required to reproduce the dynamic rupture earthquake sequence scenarios can be downloaded from (56). We provide detailed README files summarizing the data and data formats provided. **License information:** Copyright © 2023 the authors, some rights reserved; exclusive licensee American Association for the Advancement of Science. No claim to original US government works. <https://www.science.org/about/science-licenses-journal-article-reuse>

## SUPPLEMENTARY MATERIALS

[science.org/doi/10.1126/science.adi0685](https://doi.org/10.1126/science.adi0685)  
Materials and Methods  
Figs. S1 to S28  
Tables S1 and S2  
References (57–112)  
Movies S1 to S3

Submitted 1 April 2023; accepted 19 July 2023  
Published online 3 August 2023  
10.1126/science.adi0685



## The complex dynamics of the 2023 Kahramanmara#, Turkey, $M_w$ 7.8-7.7 earthquake doublet

Zhe Jia, Zeyu Jin, Mathilde Marchandon, Thomas Ulrich, Alice-Agnes Gabriel, Wenyan Fan, Peter Shearer, Xiaoyu Zou, John Rekoske, Fatih Bulut, Asl# Garagon, and Yuri Fialko

*Science* **381** (6661), . DOI: 10.1126/science.adi0685

### Editor's summary

The Kahramanmara# earthquake sequence in Turkey on 6 February 2023 caused a tremendous amount of damage and loss of life. The sequence occurred across several faults, including and associated with the East Anatolian Fault, a strike-slip fault that has had many major earthquakes in the past. Jia *et al.* used an array of geophysical observations to produce models of how the ruptures occurred. The earthquake sequence ruptured at least six faults, including a large portion of the East Anatolian Fault. The rupture sequence was complex and contained surprises in the details of how the rupture occurred. These observations and models are important for understanding strike-slip faults and forecasting seismic hazards. —Brent Grocholski

### View the article online

<https://www.science.org/doi/10.1126/science.adi0685>

### Permissions

<https://www.science.org/help/reprints-and-permissions>

Use of this article is subject to the [Terms of service](#)

---

*Science* (ISSN 1095-9203) is published by the American Association for the Advancement of Science, 1200 New York Avenue NW, Washington, DC 20005. The title *Science* is a registered trademark of AAAS.

Copyright © 2023 The Authors, some rights reserved; exclusive licensee American Association for the Advancement of Science. No claim to original U.S. Government Works



## Supplementary Materials for

### **The complex dynamics of the 2023 Kahramanmaraş, Turkey, $M_w$ 7.8-7.7 earthquake doublet**

Zhe Jia *et al.*

Corresponding author: Zhe Jia, z5jia@ucsd.edu

*Science* **381**, 985 (2023)  
DOI: 10.1126/science.adi0685

#### **The PDF file includes:**

Materials and Methods  
Figs. S1 to S28  
Tables S1 and S2  
References

#### **Other Supplementary Material for this manuscript includes the following:**

Movies S1 to S3

## Materials and Methods

### InSAR and GNSS observations

We use Synthetic Aperture Radar (SAR) data acquired by the L-band ALOS-2 satellite operated by the Japan Aerospace Exploration Agency (JAXA), and the C-band Sentinel-1A satellite operated by the European Space Agency (ESA). ALOS-2 data that cover the earthquake area include acquisitions from ascending tracks 183, 184, 185, (frames 700 and 750) and descending tracks 76, 77, and 78 (frames 2850 and 2900) made in the ScanSAR mode, and from descending track 78 made in the stripmap mode. Sentinel-1A data are acquired from ascending tracks 14, 116, and descending track 21 in TOPS mode. The respective acquisition dates are listed in Table S1.

Because of the large amplitude of coseismic slip (on the order of 10 m) and extensive surface disruption, Sentinel-1 interferograms are highly decorrelated within 10-20 km from the fault traces. Therefore, we use Sentinel-1 SAR data to calculate pixel offsets by cross-correlating the radar amplitude of full-resolution Single Look Complex (SLC) images taken before and after the  $M_w$  7.8–7.7 earthquakes. To avoid biases due to excessive filtering and averaging, especially across the fault trace, we use the raw offsets. To reduce the data scatter, we remove outliers by calculating the difference between the raw and filtered offsets. Pixels for which the difference exceeds 1 m are masked out. We do not use the azimuth offsets due to the large pixel size in the azimuth direction (~14 m), resulting in a low signal-to-noise ratio. Sentinel-1 range offsets used in our inversions are shown in Fig. S1g-i. For ALOS-2 data, we produce both interferograms (ScanSAR mode, Fig. S1a-f) and pixel offsets (stripmap mode, Fig. S1j,k).

All SAR data are processed using GMTSAR (57). Contributions to radar phase due to topography are removed using the SRTM digital elevation model (58). Interferograms are unwrapped using the branch-cut method (59). Because ALOS-2 L-band data are susceptible to ionospheric noise, we correct the latter by fitting a linear ramp to the far-field line of sight (LOS) displacements, and subtracting the respective ramps from the affected interferograms. We quality-check the data, and manually mask out identified near-field unwrapping errors in ALOS-2 interferograms (Fig. S1j,k).

We also use observations from continuous Global Navigation Satellite System (GNSS) sites located within 500 km from the epicentral area. In total, twenty-six GNSS stations are used from the CORS-TR network operated by the General Directorate of Land Registry and Cadastre, and the General Directorate of Mapping (Fig. S7). The data are sampled at 30 s intervals. The cutoff for the elevation angle is set to 10 degrees. Ten days of data are analyzed framing the mainshocks, five days before and five days after. Each day is treated as a single epoch to have the best possible accuracy except for the day of mainshocks (Feb 6, 2023). The nine hours between the two mainshocks are used to represent another epoch to differentiate between surface displacements due to each event.

The GNSS data are processed using the GAMIT/GLOBK software package in Precise Point Positioning mode (60). Fourteen IGS stations are used to achieve stabilization based on the ITRF 2014 reference frame. IGS orbits are obtained from the Scripps Orbit and Permanent Array Center (SOPAC, <http://sopac-csrc.ucsd.edu>). Earth orientation parameters are obtained from the

United States Naval Observatory (USNO, <http://usno.navy.mil>). The elevation-dependent model is applied for the receiver antenna phase center calibrations. The L1 and L2 carrier phases are combined linearly independent from the Ionosphere (LC) to eliminate the ionospheric delay. Tropospheric delays generated by the temperature, pressure, and humidity are minimized using the Global Mapping Function model in 2-hour intervals (61). The FES2004 Ocean Tide Loading (OTL) global grid is used to simulate ocean tides (62). IERS2003 is used to simulate the Earth and pole tide models (63).

We use Sentinel-1 range offsets, ALOS-2 interferograms, range and azimuth offsets from different lines of sight, and coseismic GNSS displacements to constrain the static slip distribution due to the  $M_w$  7.8-7.7 events. Because the events occurred within a short period of time, SAR data capture combined displacements due to the two events. The GNSS vector displacement data are however available for each event individually, as well as for the two events combined. The computed pixel offsets are used to map the rupture traces and, in combination with precisely located aftershocks (28), to constrain the sub-surface rupture geometry (27). Based on this analysis, we model the EAF as a vertical fault, the Nurdağı-Pazarcık Fault (NPF, fault 1 in Fig. 1A) as dipping to the northwest at 70 degrees, and the  $M_w$  7.7 rupture (the Savrun-Çardak Fault) as dipping to the north at 70 degrees. In our joint inversion, we assign relative weights of 1 to the interferograms and GNSS data, 0.6 to range offsets, and 0.2 to azimuth offsets.

For computational efficiency and better model resolution, each coseismic displacement map is sub-sampled using an iterative quad-tree sampling algorithm (64). Given the patch length of ~2 km in the shallowest part of the slip model, we sample the near-field data with a minimum spacing between the data points of about 300 to 400 meters. The unit-look vectors are computed by averaging the original values in the same groups of pixels as used for sub-sampling the phase and pixel offset data.

We extend the rectangular segments approximating the fault geometry to a depth of 30 km and several kilometers along the fault strike beyond the mapped fault traces. Each segment is divided into patches with sizes that increase with depth in a geometric progression to ensure that the model resolution matrix is close to diagonal (65). We apply positivity constraints to the strike-slip components, such that slip is constrained to be left-lateral on most of the fault segments, except for segment 5 of the  $M_w$  7.7 rupture (see Fig. 1B) which is allowed to be right-lateral. The dip-slip components are unconstrained. To prevent large variations in slip between neighboring fault patches, we apply continuity constraints (which on a regular grid are equivalent to minimizing the first spatial derivative of slip). We further impose a “soft” zero-slip boundary condition at the fault edges, except at the Earth’s surface (27).

The inversions are performed using the Green’s functions for both a homogeneous and layered elastic half-space (66). Unless noted otherwise, results presented in this manuscript correspond to layered elastic half-space models. We estimate the depth distribution of elastic moduli of the layered half-space from the 3D seismic tomography models (23). Inversions in which the fault dip angle was allowed to vary confirm a 70-degree northward dip for the  $M_w$  7.7 fault rupture, a 70-degree westward dip for the Nurdağı-Pazarcık Fault that initiated the  $M_w$  7.8 event, and a vertical dip on all ruptured sections of the EAF. Figs. S3–S6 show the sub-sampled data, predictions of the best-fit models and residuals for the data sets used in the inversion. Overall,

our preferred model (Figs. 1B and S2) fits the main features of the displacement field well, with a variance reduction of more than 96% for the interferograms and 75% for the pixel offsets. We compute the seismic moment for each event by summing up scalar seismic moments of the respective slip patches (Figs. 1B and S2). Inversions using a homogeneous half-space give rise to the moment magnitudes of 7.83 and 7.70 for the first and second event, respectively, assuming the shear modulus of 33 GPa. Inversions using a layered half-space give rise to the moment magnitudes of 7.89 and 7.74 for the first and second event, respectively, assuming the depth-dependent shear modulus from our layered model. Fig. S7 shows a comparison between GNSS observations and model predictions for each event. Since the static slip model was derived from data spanning both events, a good agreement between the data and model predictions for individual events (Fig. S7) indicate that the latter are well resolved and trade-offs between coseismic displacements due to individual events in our inverse models are minimal. We note that models assuming a layered elastic half-space do a better job fitting both the near- and far field GNSS data compared to models assuming a homogeneous elastic half-space, in agreement with studies of other large earthquakes (26).

### Subevent inversion

We apply a subevent inversion method (30, 31) to simultaneously constrain a total of 6 subevents for the  $M_w$  7.8 earthquake and 4 subevents for the  $M_w$  7.7 earthquake. We determine the number of subevents by iteratively adding subevent numbers in the inversions until the waveforms are well fit and the total moment is consistent with the long-period moment from the geodetic solutions. The major advantage of the subevent inversion method is that it can describe multi-fault rupture processes with flexible subevent locations, timings, and focal mechanisms, without imposing strong assumptions on the fault geometry or rupture velocity.

Each subevent has 10 unknown source parameters, including the horizontal location and depth, centroid time, centroid duration, and 5 deviatoric moment tensor components. Our two-stage algorithm allows us to search for part of these parameters nonlinearly and invert the data for the other parameters using a linear approach, which substantially improves the inversion efficiency. In the outer (first) stage, we use a Metropolis-Hasting Markov Chain Monte Carlo (MCMC) sampler to drive the search for nonlinear parameters, including subevent locations, timings, and source durations. In each MCMC sampling step, we perturb one of the nonlinear parameters while keeping the other nonlinear parameters at their current values (67), which ensures a high acceptance rate and sampling efficiency. Given the set of nonlinear parameters in the inner (second) stage, we linearly invert the seismic data for the moment tensors by extending their linear relationship (68) to multiple sources. Ultimately, the MCMC sampler only needs to search 5 nonlinear parameters for each subevent, which clears the path to extensively explore the model space.

We generate 192 Markov Chains and eventually keep the best 48 for each inversion, to avoid the chains being trapped in local minima. Our MCMC inversion incorporates a Bayesian framework that accounts for data errors and model priors to estimate the model uncertainties. We assign bounded uniform prior distributions of all nonlinear parameters except the horizontal locations, for which we set priors based on the aftershock distributions. Although the actual noise and instrumental errors for the seismic waveforms are minimal, we empirically introduce a data error of 10% of the misfit to address inaccurate assumptions of the wave propagation processes

(Green's function). The model uncertainties are ultimately represented by the widths of the Markov Chain sample distributions, which are equivalent to the posterior probability density functions.

We incorporate a variety of datasets, including P waves of 63 teleseismic (epicentral distance between 30°-90°) stations in displacement and velocity, SH waves of 66 teleseismic stations in displacement, and three-component full waveforms in velocity recorded by 78 local (epicentral distance within 200 km) strong ground motion stations (Fig. S9-S13). The data are selected from the Global Seismic Network (GSN), the International Federation of Digital Seismograph Network (FDSN), as well as the Turkish National (TK) strong ground motion network for good quality and azimuthal coverage. The weighting of these datasets is set to be 5, 1, and 0.0015 for similar contributions to the final misfit. We remove the instrument responses and the linear trends of these data. For the teleseismic data, we rotate the two horizontal components to the radial and transverse components, and we apply a 0.005–0.15 Hz band-pass filter. For the local strong ground motion data, we apply a 0.02–0.15 Hz filter. To account for path effects and picking errors, we allow a time shift up to 2s for teleseismic P waves, 5s for teleseismic SH waves, and 2s for the regional strong motion data. We calculate Green's functions using the 1D velocity model of Güvercin et al. (23) for the crust (Table S2) and the IASPEI91 model (69) for the deeper earth. We compute teleseismic Green's functions with a hybrid method that combines a propagator matrix and ray theory (70, 71), and calculate local Green's functions based on the frequency-wavenumber integration method (72).

The seismicity locations and the space geodesy data tightly constrain the fault geometry and surface ruptures, which provides our subevent inversion with useful priors. For the  $M_w$  7.8 earthquake, we incorporate the horizontal spatial density of its early aftershocks before the  $M_w$  7.7 event as the prior distribution for the subevent locations. We also fix the location of the first subevent to be at the hypocenter on the NPF, which is well constrained by the InSAR data. For the  $M_w$  7.7 earthquake, we impose the horizontal spatial density of its aftershocks as the prior for the subevent locations, and anchor the last subevent at the location where the slip patch on the Doğanşehir branch is observed in the static slip model. Fixing the location of one subevent avoids all subevents moving their horizontal locations together with the seismograms shifting simultaneously, thus stabilizing the inversion. The narrow subevent model uncertainty limits for the  $M_w$  7.8 and 7.7 events reveal that their subevent models are well constrained by the data.

### Back projection

We employ a standard time-domain back-projection method (32, 73) to analyze the rupture propagation of the  $M_w$  7.8 earthquake. This technique has been widely used to detect aftershocks and resolve earthquake radiation patterns because it does not make many assumptions about the fault geometry or rupture velocity (9, 74). Back-projection has successfully investigated the spatiotemporal evolution of complex earthquakes, such as multi-fault rupture events and supershear earthquakes (75, 76).

We collect P-wave velocity records of the event from all seismic stations within an epicentral distance range of 30° to 90°. We apply a 0.05–0.5 Hz fourth-order Butterworth filter to the data and remove records with signal-to-noise ratios (SNR) of less than 3. The SNR is calculated as the root-mean-square (RMS) amplitude ratio from time windows 10 s before and after the

theoretical P-wave arrival obtained from the International Association of Seismology and Physics of the Earth's Interior (IASP91) travel-time tables (69). To eliminate any effects of stations located close to the nodal plane directions, we exclude them from the analysis. We visually inspect the records and select only those with clear P-wave onsets. Traces with positive polarities are also discarded. After quality control, we align the traces using multi-channel cross-correlation with a time window from -2 to 6 s relative to the theoretical P arrivals. Polarity flips are not allowed during cross-correlation. In total, we use 391 stations to image the rupture evolution of the  $M_w$  7.8 earthquake, as shown in Fig. S15.

The back-projection procedure first predefines a set of points for potential sources around the earthquake hypocenter, with a fixed horizontal point spacing of 10 km at the hypocentral depths (Point-set 1). The potential source point spans an area of 600 km by 600 km, with the earthquake epicenter located at the center of the points. To improve the spatial resolution of the back-projection images, we employ a  $N$ th root stacking ( $N=4$ ) method, albeit at the cost of losing absolute amplitude information (77, 78). We normalize the records using their peak amplitudes and inversely scaling by the number of contributing stations within  $5^\circ$  to balance the azimuthal and spatial coverage of the stations. To evaluate the spatiotemporal migration, we generate back-projection snapshots using different stacking windows to balance the trade-off between resolution and robustness (Fig. S15). We normalize the back-projection snapshots by the maximum power within each window and present them as contours with coherence exceeding 90% of the maximum normalized energy (Fig. S15). The back-projection snapshots exhibit good agreement with the fault traces. Since the event displays simple linear rupture propagation, we estimate the average rupture speed of various rupture branches to be approximately 3 km/s for the  $M_w$  7.8 earthquake.

The  $M_w$  7.8 earthquake ruptured a group of nearly vertical strike-slip faults, and space geodetic observations enable us to accurately define the fault traces. To limit the potential sources, we restrict them to be along the fault traces (Point-set 2) for the back-projection analysis. We adopt the same stacking procedure using the same set of P waves as in Point-set 1. The results, presented in Fig. 2, include snapshots with varying window lengths that help to infer the earthquake rupture propagation. The back-projection images are robust and in agreement with those obtained using Point-set 1.

### Kinematic slip inversion

We conduct a joint kinematic slip inversion of the  $M_w$  7.8 and 7.7 earthquakes using both seismic and geodetic data, following the finite-fault inversion framework of Jia et al. (33). We used the same fault geometry as used in the static slip inversion (Figs. 1B, S2). The rake angles are constrained by the corresponding subevent focal mechanisms (rake angles of fault 1-6:  $0^\circ$ ,  $8^\circ$ ,  $0^\circ$ ,  $-10^\circ$ ,  $180^\circ$ ,  $40^\circ$ ). We discretize each fault segment into subfault grids with horizontal and depth intervals of 6 km and 4 km, respectively. Each subfault grid has a triangle moment rate function with a duration of 4 s.

For both events, we use one rupture velocity per fault segment, and calculate the rupture time of each subfault patch based on its in-plane distance from the grid of initial rupture (i.e., the epicenter on the first segment), which is effectively a slip-pulse rupture expansion. For bilateral rupture scenarios, estimation of rupture velocity based on subevent locations may be biased.

Through grid-searching (Fig. S18), we obtain the optimal rupture velocities of 3.2 km/s to the northeast and 2.8 km/s to the southwest for the  $M_w$  7.8 earthquake. Notably, a delay for the nucleation of the southwest segment is required by the data, and we find the optimal delay time is 10 s (Fig. S17). For the  $M_w$  7.7 earthquake, we obtain an eastward rupture velocity of 2.5 km/s, whereas we constrain a westward supershear rupture with an optimal velocity of 4.5 km/s (Fig. S19). Unlike the  $M_w$  7.8 event, we do not find that any delayed rupture branches occurred during the  $M_w$  7.7 earthquake.

Once we define the fault geometries, rake angles, and rupture times, the slip amplitudes are the only remaining unknown parameters. We extend the linearized finite-fault inversion method of Hartzell and Heaton (79) to model the two earthquakes in a single inversion. We use a combination of regional strong ground motions, teleseismic P and SH waves in displacement, two tracks of ALOS-2 ScanSAR line-of-sight displacements, and the Sentinel-1 ascending and descending range offsets. Processing and filtering of the seismic data and the Green's functions follows the same procedures as the subevent inversion described above, but we do not allow any time shifts for the local strong motion waves to avoid trade-offs between time-shifting and rupture velocity estimates. Processing of the InSAR data follows the previous static slip inversion. InSAR Green's functions are calculated using the same 1D velocity model of Güvercin et al. (23) with a frequency-wavenumber integration method (72).

We set up a linear system describing the relationship between observed data and the subfault synthetics,

$$\begin{bmatrix} G_{SM\_7.8}^1 & G_{SM\_7.8}^2 & \cdots & G_{SM\_7.8}^k & 0 & 0 & \cdots & 0 \\ G_{TelP\_7.8}^1 & G_{TelP\_7.8}^2 & \cdots & G_{TelP\_7.8}^k & 0 & 0 & \cdots & 0 \\ G_{TelSH\_7.8}^1 & G_{TelSH\_7.8}^2 & \cdots & G_{TelSH\_7.8}^k & 0 & 0 & \cdots & 0 \\ 0 & 0 & \cdots & 0 & G_{SM\_7.7}^1 & G_{SM\_7.7}^2 & \cdots & G_{SM\_7.7}^l \\ 0 & 0 & \cdots & 0 & G_{TelP\_7.7}^1 & G_{TelP\_7.7}^2 & \cdots & G_{TelP\_7.7}^l \\ 0 & 0 & \cdots & 0 & G_{TelSH\_7.7}^1 & G_{TelSH\_7.7}^2 & \cdots & G_{TelSH\_7.7}^l \\ G_{InSAR\_7.8}^1 & G_{InSAR\_7.8}^2 & \cdots & G_{InSAR\_7.8}^k & G_{InSAR\_7.7}^1 & G_{InSAR\_7.7}^2 & \cdots & G_{InSAR\_7.7}^l \end{bmatrix} * \begin{bmatrix} m_{7.8}^1 \\ m_{7.8}^2 \\ \vdots \\ m_{7.8}^k \\ m_{7.7}^1 \\ m_{7.7}^2 \\ \vdots \\ m_{7.7}^l \end{bmatrix} = \begin{bmatrix} d_{SM\_7.8} \\ d_{TelP\_7.8} \\ d_{TelSH\_7.8} \\ d_{SM\_7.7} \\ d_{TelP\_7.7} \\ d_{TelSH\_7.7} \\ d_{InSAR\_both} \end{bmatrix}$$

in which  $\mathbf{m}_{7.8}^{1\dots k}$  and  $\mathbf{m}_{7.7}^{1\dots l}$  are the slip vectors of all subfault grids for the  $M_w$  7.8 and  $M_w$  7.7 earthquakes, respectively,  $\mathbf{d}_{[data\ type]_{[event]}}$  is the data vector including a variety of data types (Strong motion, teleseismic P and SH waves, and InSAR).  $\mathbf{G}_{[data\ type]_{[event]}}^{1\dots[k\ or\ l]}$  represents the synthetics of different data types for unit slip on the corresponding subfault grids. For the seismic data, both  $\mathbf{G}$  and  $\mathbf{d}$  are time series of all stations from end to end, and they are linked to the  $M_w$  7.8 and 7.7 earthquakes independently. The InSAR data and Green's functions are formatted as gridded surface line-of-sight (LOS) displacements and they span both earthquakes. Therefore, the seismic data helps to differentiate the slip distribution for these two events, while the InSAR data provide constraints on their total slip. We can directly resolve the least-square slip distributions of the two earthquakes, but the result is unstable because of ill-conditioning of this inverse problem. To stabilize the inversion, we introduce four types of constraints, including 1) non-negative constraints on the slip, 2) minimization of the slip differences between adjacent subfault grids, 3) penalizing slip at the non-surface boundaries of the faults, and 4) minimizing the L2 norm of the slip distribution (79, 80). These constraints help to avoid unphysical solutions

(negative slip, enormous strain, etc.) and overfitting. To flexibly incorporate these constraints, we used the CVX optimization algorithm (81) to solve our inverse problem.

### Dynamic rupture simulations

Dynamic rupture models require prescribed initial conditions, including fault geometry, relative fault strength, prestress, and material properties (82, 83). Our dynamic rupture simulations use the same model setup for linked forward simulations of both earthquakes (54). We inform our initial parameterization from observations: fault geometry from geodesy and seismicity, large-scale fault loading from regional seismo-tectonics and smaller-scale stress heterogeneity from static slip inversion, and fault strength from first-order earthquake kinematics. We prescribe larger fracture energy, larger nucleation area, and closer to critically stressed faults for the second event to capture its rupture dynamics which are distinct from the first earthquake (see main text).

#### Fault geometries:

We account for the large-scale geometrical complexities of the fault system, including fault bends and secondary segments. Our dynamic rupture model includes the faults hosting both events and the relative effects of the static and dynamic stresses of the  $M_w$  7.8 event on the dynamics of the second earthquake. We include ten curved, intersecting segments of the EAF and SCF (Fig. S20) as inferred from geodetic analysis and resembling the fault geometries of the static and kinematic models. We extend mapped surface fault traces to a depth of 20 km with varying dip angles ranging between  $90^\circ$  for all EAF segments and  $70^\circ$ N for the main segments of the second event. The minor Gökşun splay (segment 5, Fig. 1) is dipping  $90^\circ$ .

#### Fault friction and relative fault strength:

We use the widely used linear slip-weakening friction law (84), with static friction coefficient  $\mu_s=0.6$  and dynamic friction coefficient  $\mu_d=0.2$  on all faults. The critical slip distance varies between  $D_c=0.5$  m for faults hosting the first earthquake and for the Gökşun splay, and  $D_c=1.0$  m, implying larger fracture energy for the main faults hosting the second event.

$S$ , the ratio of initial strength excess to nominal stress drop (85), is a measure for the relative strength of faults in dynamic rupture simulations. While static and dynamic friction coefficients are constant on all faults, we find that prescribing variable relative fault strength  $S$  is required to dynamically reproduce the first-order earthquake kinematics, such as moment magnitude and rupture extent.  $S$  varies due to variable prestress (next section). Furthermore, the local fault geometry modulates the prescribed regionally variable relative fault strength (Fig. S20), implying that locally more optimally oriented fault portions are closer to critically prestressed.

#### Prestress:

We combine large-scale variability in fault loading inferred from regional seismo-tectonics and modulated by fault geometry with small-scale heterogeneity inferred from static slip inversion. We assume depth-dependent effective normal stress and combine shallow mildly over-

pressurized pore fluids, with a pore fluid pressure of  $\nu = \rho_{\text{water}}/\rho = 0.66$ , with effectively constant effective normal stress below  $\sim 6\text{km}$  (86-88).

Following previous dynamic rupture simulations unraveling complex multi-fault earthquakes (12, 54, 89, 90), we constrain large-scale variability in fault loading from regional seismotectonic observations (Fig. S20). Here we combine stress inversion (23), InSAR constrained principal strain rate orientations (91), with recent focal mechanisms (AFA, <https://depem.afad.gov.tr/event-focal-mechanism>) to prescribe an along-strike rotating prestress state, which is required to dynamically reproduce rupture dynamics of both earthquakes. Specifically, we find that close-to-optimal loading of the central segment of the second earthquake reproduces its observed large slip and surface displacements.

Small-scale variability of dynamic rupture parameters cannot be measured in situ and is difficult to constrain. Dynamic source inversions for friction parameters and the initial state of fault stress (92, 93) are limited to sufficiently simple dynamic rupture models due to the computational cost of the forward problem. We derive the spatially-variable static stress changes associated with our geodetically inferred static-slip model using the same computational model as the dynamic rupture models. In a pseudo-dynamic calculation, we impose the geodetic slip model and measure the associated stress heterogeneity (37) in the full stress tensor.

Inferring initial stresses directly from data-driven slip models (94, 95) often requires additional assumptions and ignores regional tectonic constraints. We combine large-scale and small-scale prestress heterogeneities based on a few trial dynamic rupture scenarios. We find that balancing their respective amplitudes using a scaling factor of 0.65 for the smaller-scale stress changes and  $S$  ratios varying between 0.54 and 2.33 (Fig. S20) spontaneously reproduces earthquake kinematics, geodetic deformation and ground motions of both events very well (Figs. S21-S25).

#### Nucleation:

We initiate both ruptures by linearly decreasing static frictional strength  $\mu_s=0.6$  to  $\mu_d$  in two separately-activated gradually expanding nucleation patches of maximum sizes 2 km ( $M_w$  7.8) and 3 km ( $M_w$  7.7) centered at the same respective hypocenter locations as in the kinematic model and observationally inferred from AFAD (53). Only a critical portion (96) of the fault needs to reach failure to nucleate rupture, while other parts of the faults are prestressed well below critical and yet break dynamically. We use a nucleation patch smoothly varying in space and time (97) and acting across a minimal-sized perturbation area, avoiding artifacts when initiating self-sustained spontaneous rupture with minimal perturbation determined in several trial dynamic rupture simulations.

#### Material properties and dynamic rupture model domain:

We embed all faults in the same 1D velocity model as the data-driven models (23), which does not include viscoelastic attenuation. Our dynamic rupture model domain accounts for high-resolution (450 m) topography from SRTM DEM data (58). We assume a depth-dependent, non-associated Drucker-Prager elasto-viscoplastic rheology to model coseismic off-fault plastic deformation (98). We parameterize off-fault plasticity by bulk internal friction coefficient and 3D variable plastic cohesion. We use a uniform bulk friction coefficient of 0.6, matching our on-

fault static friction coefficient, and define plastic cohesion  $C_{\text{plast}}$  as proportional to the 1D depth-dependent shear modulus  $\mu$  in [Pa] following Roten et al. (99), as:

$$C_{\text{plast}} = 2 \times 10^{-4} \max(\mu(z), 2 \times 10^{10})$$

We taper bulk cohesion at depths shallower than 2 km, where confinement stresses are low.

Numerical method:

We solve the spontaneous dynamic rupture problem with high-order accuracy in space and time using the open-source software SeisSol ([www.seissol.org](http://www.seissol.org)). SeisSol uses the Arbitrary high-order accurate DERivative Discontinuous Galerkin method (ADER-DG) (100) and end-to-end optimization for high-performance computing infrastructure (101-103). SeisSol employs fully non-uniform unstructured tetrahedral meshes that statically adapt to geometrically complex 3D geological structures, such as non-planar, intersecting faults, and topography. SeisSol has been verified in various community benchmarks (97, 104).

We spatially discretize our model domain in an unstructured tetrahedral mesh of 31 million tetrahedral elements. The mesh is statically adapted to resolve frequencies of at least 1 Hz everywhere in a high-resolution area of 400 km  $\times$  200 km with the NE-SW main axis aligned with the fault system, acknowledging the 1D seismic velocity model at depth. In larger distances to the faults, mesh resolution adaptively coarsens. We still resolve 0.25 Hz at the edges of the dynamic rupture model domain which spans a total extent of 600 km  $\times$  600 km  $\times$  500 km. We choose a maximum element edge-length of 300 m at all fault interfaces. The size of the area behind the rupture front where shear stress decreases from its static to its dynamic value is the process zone width (105). We here measure the median process zone width as 530 m (98). Our rupture models are well resolved by our chosen spatial and temporal discretization, which includes basis functions of polynomial order  $p = 4$ , noting that each dynamic rupture element provides sub-element resolution.

$\Delta\text{CFS}$  and  $\Delta\text{CFD}$  calculations:

We compute  $\Delta\text{CFS}$  or  $\Delta\text{CFD}$  across the SCF fault system from the dynamic rupture simulation of the  $M_w$  7.8 earthquake, which allows us not to be restricted to an a priori assumed planar fault geometry but to use a full cartesian tensor and account for the full complexity of the fault network when resolving on-fault stress changes. We calculate the  $M_w$  7.8 static Coulomb failure stress changes  $\Delta\text{CFS}$  at 150 s after initiating the first dynamic rupture simulation, which ensures that transient seismic waves have left the model domain. We measure  $\Delta\text{CFS}$  in the direction of maximum shear tractions at each point of the complex fault system as  $\Delta\text{CFS} = \Delta\tau - f \Delta\sigma_n$ , with  $\Delta\tau$  and  $\Delta\sigma_n$  being the dynamic shear and normal fault stress changes, and  $f = \mu_s = 0.6$  the static friction coefficient used in the dynamic rupture simulations. We measure the absolute dynamic Coulomb failure stress perturbation ( $\Delta\text{CFD}$ ) in the direction of maximum initial traction

throughout the rupture time of the first event's dynamic rupture scenario. We show its maximum values across the SCF fault system in Fig. 4C of the main text.

To investigate the sensitivity of the computed static stress changes to uncertainties in the orientation of the nucleation site of the  $M_w$  7.7 event, we compute shear and normal stress perturbations caused by the  $M_w$  7.8 mainshock on fault strikes ranging from 0 to 360 degrees, assuming a vertical dip (Supplementary Video S3). Calculations are performed using the best-fit static slip model of the  $M_w$  7.8 event constrained by SAR and GNSS data (Figs. S1 and S7), and the boundary element code DIS3D (106, 107). Fig. S27 shows the computed perturbations in the shear, normal, and Coulomb stress (assuming the coefficient of friction of 0.6) on faults striking slightly north of west, similar to the orientation of the Çardak fault that hosted the nucleation of the  $M_w$  7.7 event. The latter was encouraged by both the normal and shear static stress changes. Note that the Coulomb stress change is positive along a potential rupture path toward the EAF (a straight eastward continuation of the Çardak-Sürgü fault), unlike the actual rupture path along the Doğanşehir fault that experienced a decrease in the Coulomb stress (see Fig. 4D and Video S3).

#### Rupture velocity analysis using near-fault strong motion pulses

The SW part of the EAF is well instrumented with 16 stations located nearly on top of the fault trace. Records from these stations can thus be used to track the passage of the rupture and estimate the rupture speed. To that end, we first band-pass filter the strong motions between 0.01-1 Hz and hand-pick the onset timing of the strong pulse that marks the rupture passage. Knowing the distance between the stations, we then estimate the average rupture speed using a linear regression. We also use this approach on the ground motions predicted by our dynamic rupture model to further compare our dynamic rupture model with the observations. From the observed strong ground motions, we estimate a rupture speed of 3.25 km/s and 2.94 km/s on the EW and NS component respectively, leading to an average rupture speed of 3.10 km/s. For the modeled ground motion, we estimate an average rupture speed of 2.97 km/s (2.975 km/s on the EW component and 2.971 km/s on the NS component). This is consistent with the 2.8 km/s solution derived from our kinematic slip inversion, confirming an overall subshear rupture on the SW part of the EAF.

#### Ground motion analysis

We compute peak ground velocities (PGV) and peak ground accelerations (PGA) for both earthquakes from local strong motion acceleration recordings and from the dynamic rupture simulation which resolves frequencies up to 1.0 Hz in a broad region of 400×200×25 km covering the fault systems of both events and nearby strong motion stations. We compute the observed PGVs and PGAs using local strong motion data obtained from AFAD (Disaster and Emergency Management Authority, 1973) using the automatically processed records for both the  $M_w$  7.8 and 7.7 earthquakes. We define PGV and PGA as the rotationally-independent geometric mean (GMRotD50, 108) of the two horizontal components of ground velocity and acceleration,

respectively. We compute the Joyner-Boore distance,  $R_{JB}$  (109), for each station using the representation of fault rupture used in the USGS ShakeMaps (110).

We compute residuals from a ground motion model (55) developed for “all seismically-active regions bordering the Mediterranean Sea and extending to the Middle East”, by taking the natural logarithm of the observational and synthetic data divided by the predictions (Fig. S23). We assume a site condition of  $VS30=760$  m/s for the residual calculation. We used the OpenQuake (111) software to obtain the ground motion model predictions.

### Captions for Animations

Video S1: Slip rate animation, dynamic rupture scenario of the  $M_w$  7.8 earthquake.

Video S2: Slip rate animation, dynamic rupture scenario of the  $M_w$  7.7 earthquake.

Video S3: Static stress changes due to the  $M_w$  7.8 earthquake on vertical strike-slip faults, as a function of strike angle, at depth of 5 km.

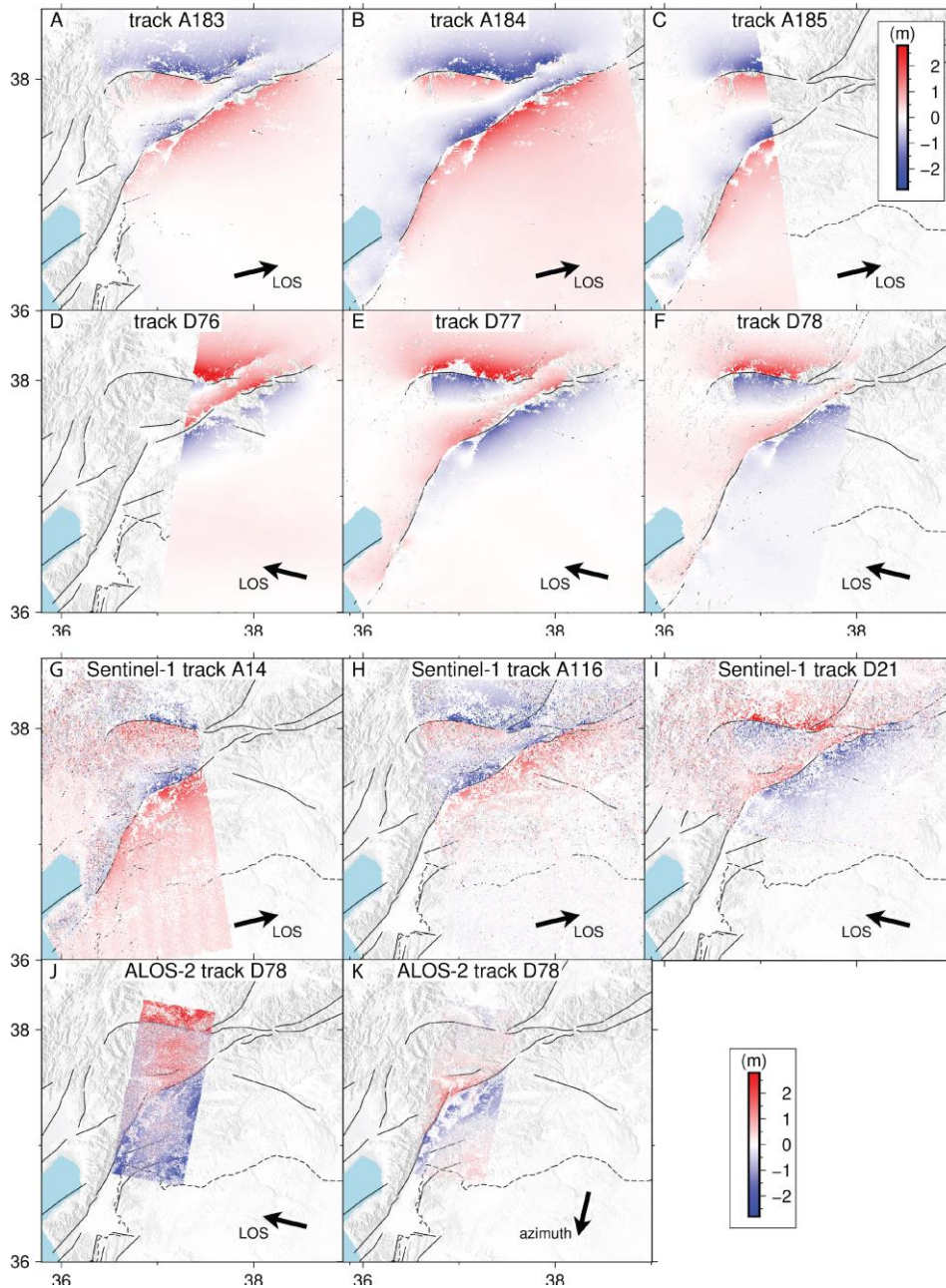


**Fig. S1.** Line of sight (LOS) displacements and pixel offsets used in this study. (a-f) LOS displacements from ALOS-2 ScanSAR interferograms from ascending tracks 183, 184, and 185, and descending tracks 76, 77, and 78. (g-jb) Range and (k) azimuth offsets derived from the TOPS SAR data from Sentinel-1 tracks A14, A116, D21 (g-i), and stripmap mode data from ALOS-2 descending track D78 (j,k). Horizontal and vertical axes represent longitude and latitude, in degrees. Colors represent displacement amplitude, in meters. Arrows denote a line of sight from the radar antenna to the ground, and a positive direction of the LOS displacements and azimuth offsets.

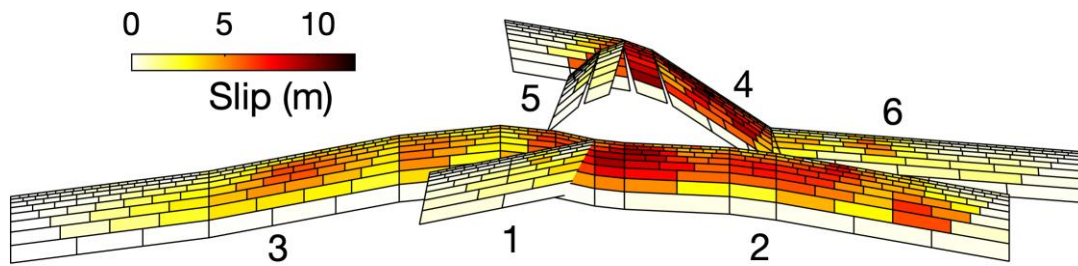


**Fig. S2.** Static slip distribution from inversions of space geodetic (SAR and GNSS) data, from a different perspective than in Fig. 1B, showing the slip distribution on fault segments 1 and 3 in greater detail. Notation is the same as in Fig. 1B.

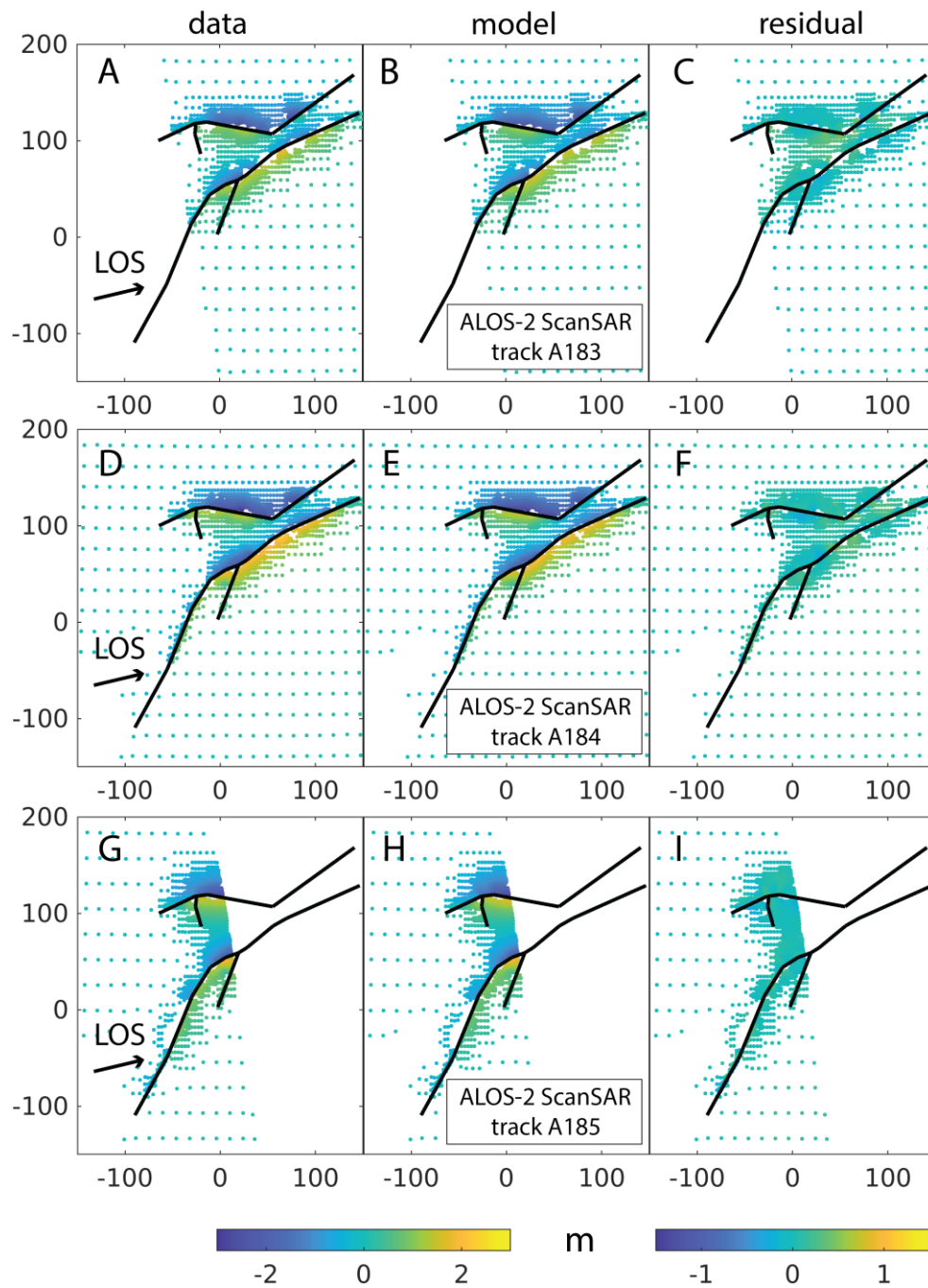


**Fig. S3.**

Sub-sampled data, model predictions and residuals for the ALOS-2 ScanSAR interferograms from the ascending tracks 183 (a-c), 184 (d-f), and 185 (g-i). Horizontal and vertical axes represent eastings and northings in local UTM coordinates, in kilometers, with origin at 37°E, 37°N. Colors represent displacements, in meters.

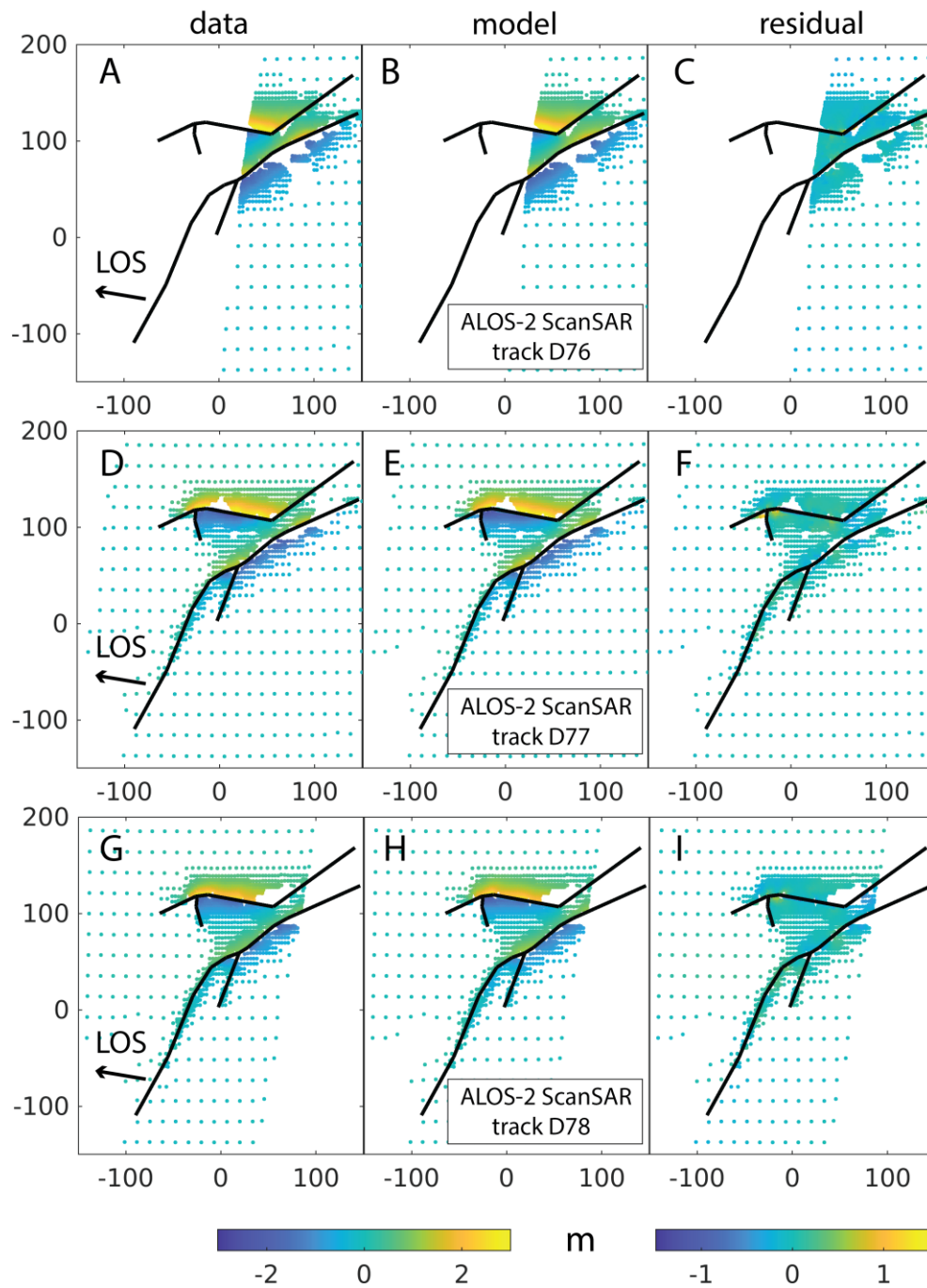


**Fig. S4.**

Sub-sampled data, model predictions and residuals for the ALOS-2 ScanSAR interferograms from the descending tracks 76 (a-c), 77 (d-f), and 78 (g-i). Horizontal and vertical axes represent eastings and northings in local UTM coordinates, in kilometers, with origin at 37°E, 37°N. Colors represent displacements, in meters.

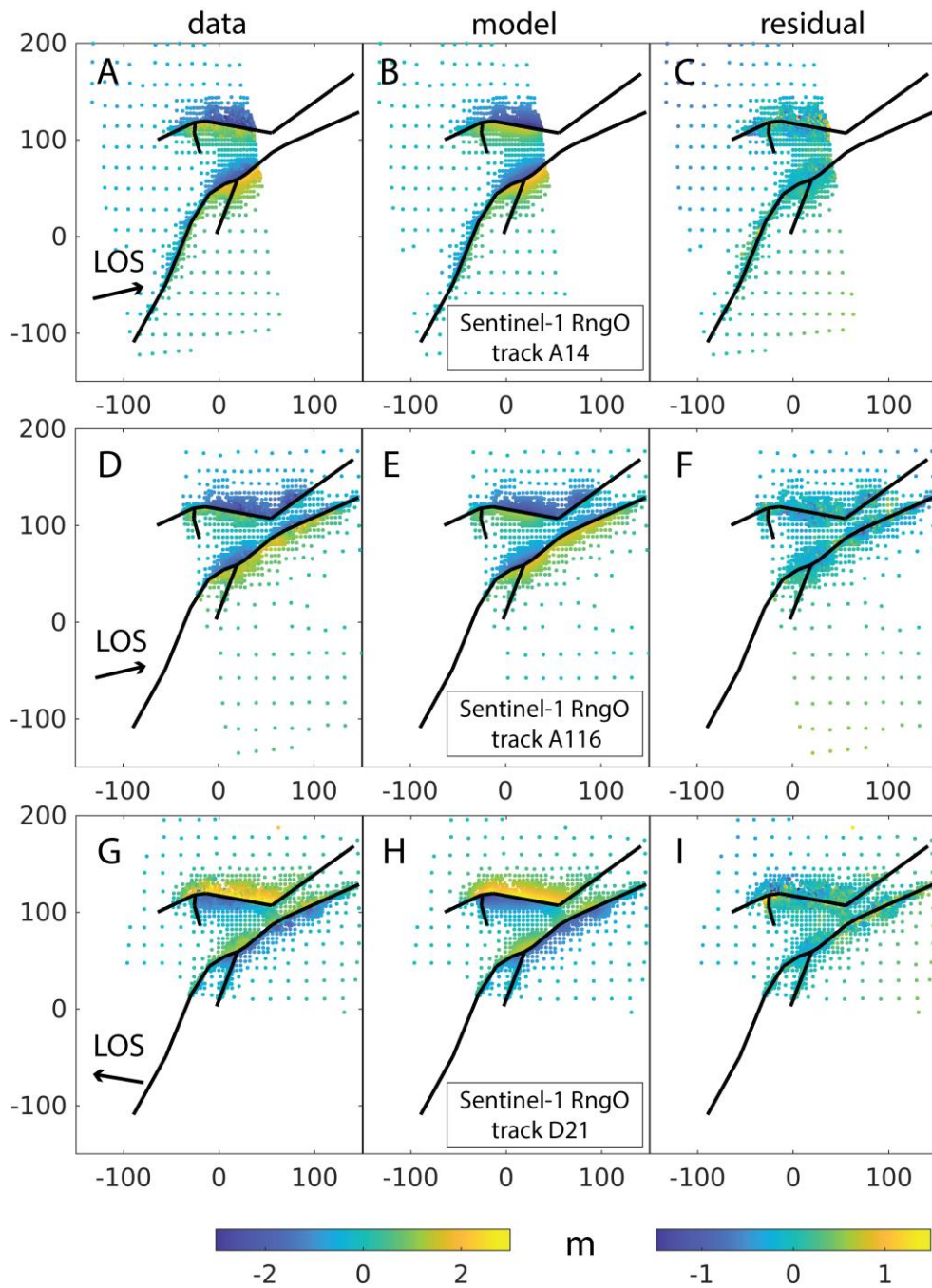


**Fig. S5.**

Sub-sampled data, model predictions and residuals for the Sentinel-1 range offsets from the ascending tracks 14 (a-c), 116 (d-f), and descending track 21 (g-i). Horizontal and vertical axes represent eastings and northings in local UTM coordinates, in kilometers. Colors represent displacements, in meters.

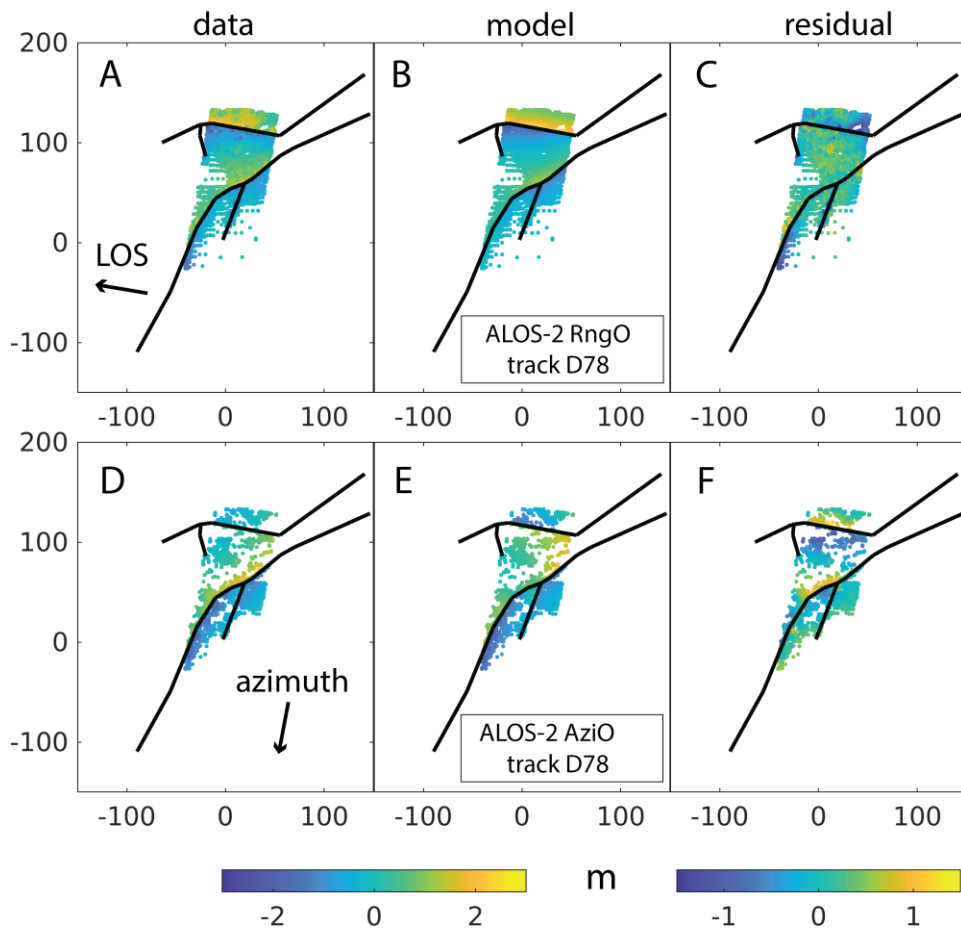


**Fig. S6.**

Sub-sampled data, model predictions and residuals for the ALOS-2 range offset (a-c) and azimuthal offset (d-f) from descending track 78. Horizontal and vertical axes represent eastings and northings in local UTM coordinates, in kilometers. Colors represent displacements, in meters.

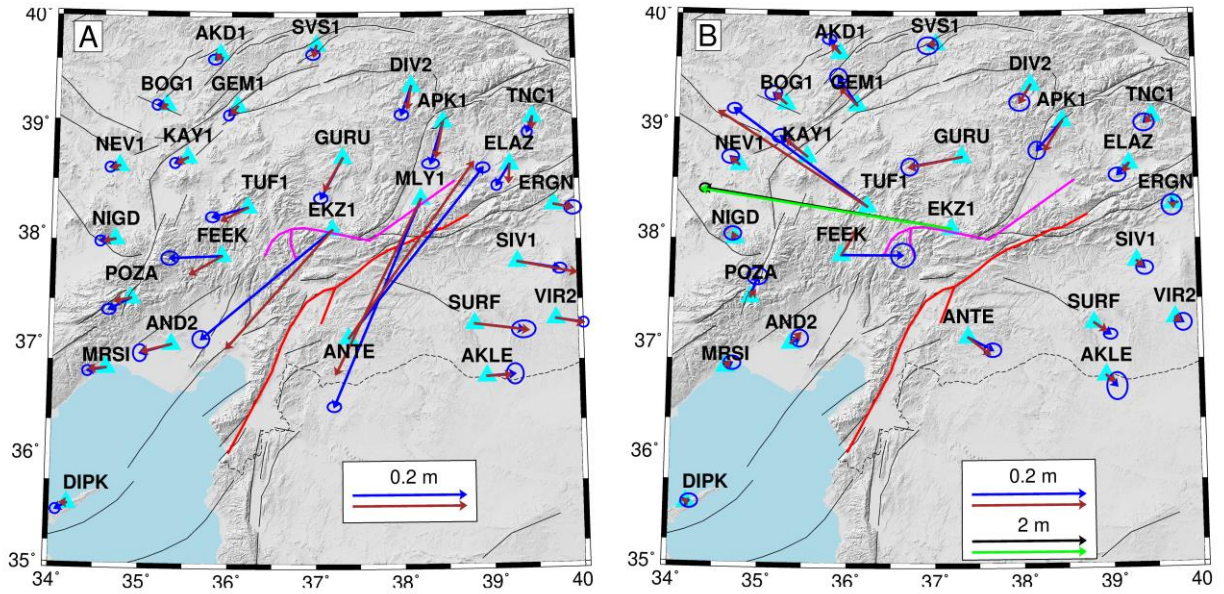


**Fig. S7.**

Comparison between GNSS observations (blue arrows) and model predictions (dark red arrows) from the  $M_w$  7.8 event (a) and the  $M_w$  7.7 event (b). In panel (b), black and green arrows represent the observed and modeled displacements at site EKZ1, which are substantially larger than displacements at all other sites, thus shown on a different scale. Ellipses denote 2-sigma errors in the displacement solutions.

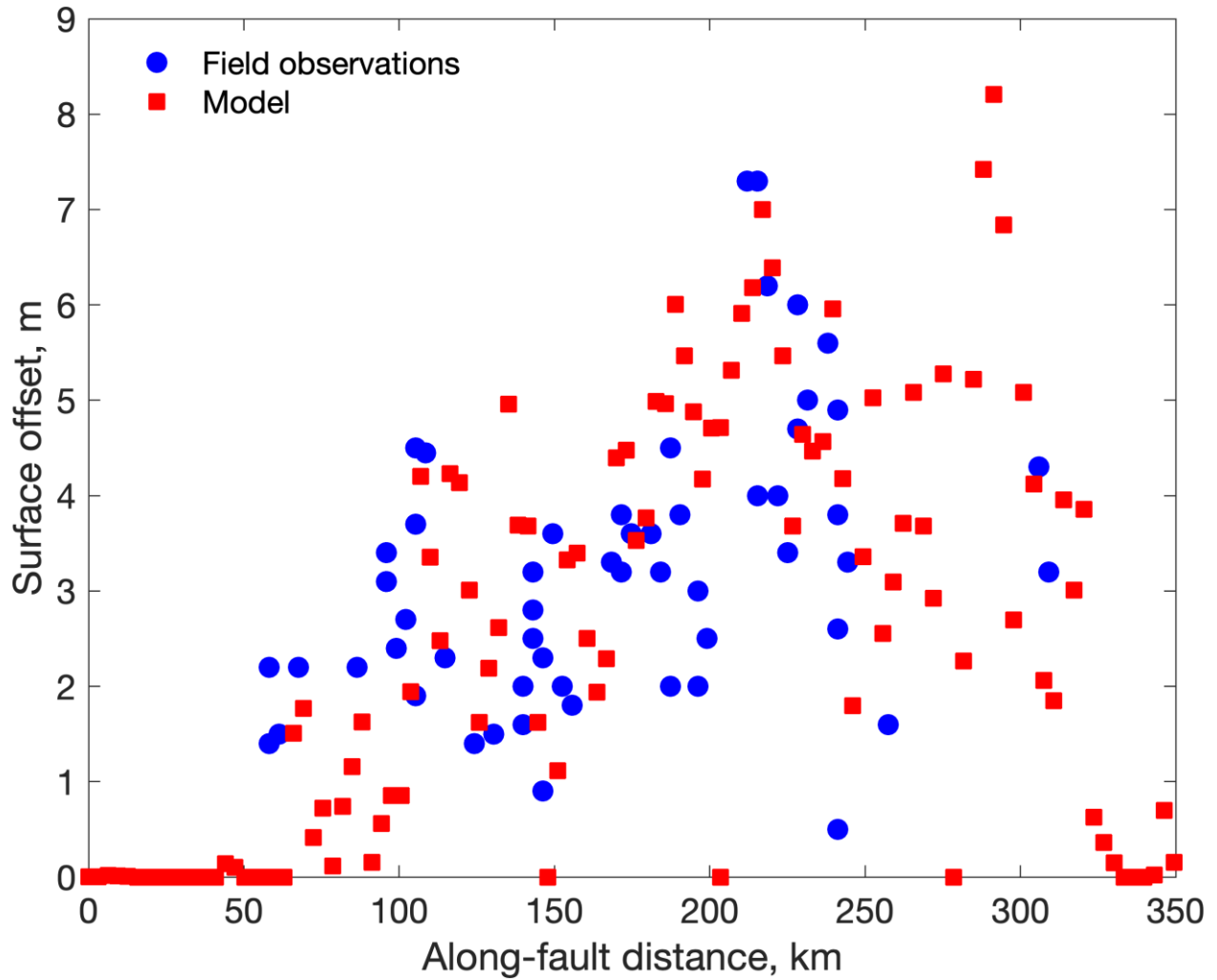
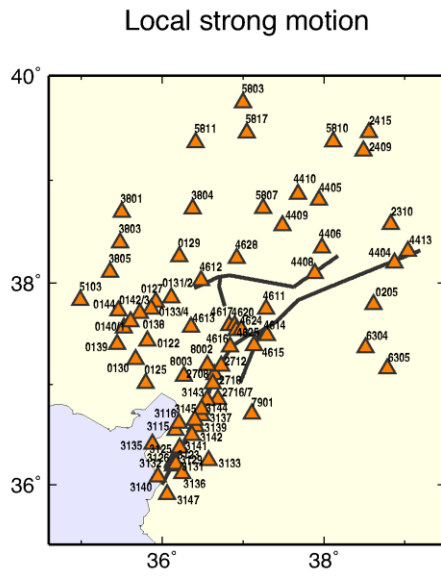


**Fig. S8.**

Comparison between the surface slip predicted by our preferred static slip model (Fig. S2) and geologically mapped surface offsets (18) for the  $M_w$  7.8 event. The along-fault profile starts at the southwestern tip of our slip model (Fig. 1B). Note that the field observations shown in this figure were not used to constrain our models. Both the model and the data suggest a considerable heterogeneity in slip amplitude along the earthquake rupture.

(a)



(b)

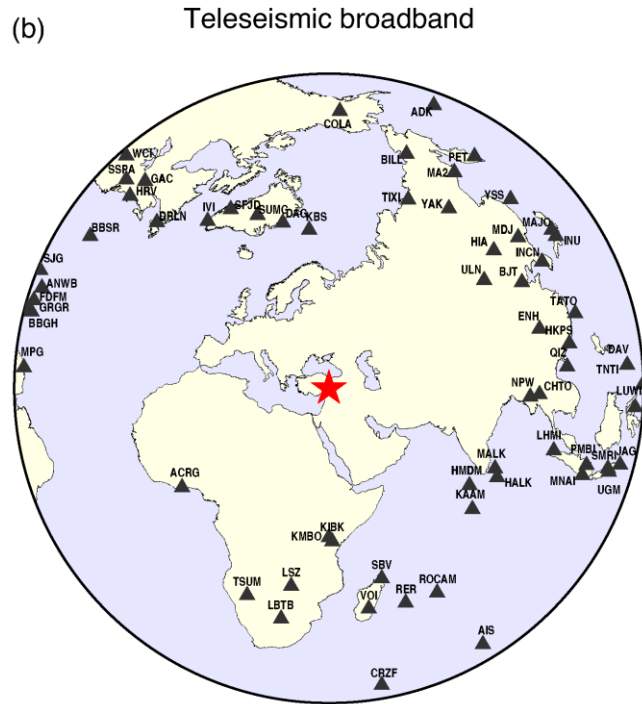


**Fig. S9.**

Seismic stations (triangles) used in the subevent and kinematic finite-fault inversions. Strong motion stations are in orange, and teleseismic stations are in black.

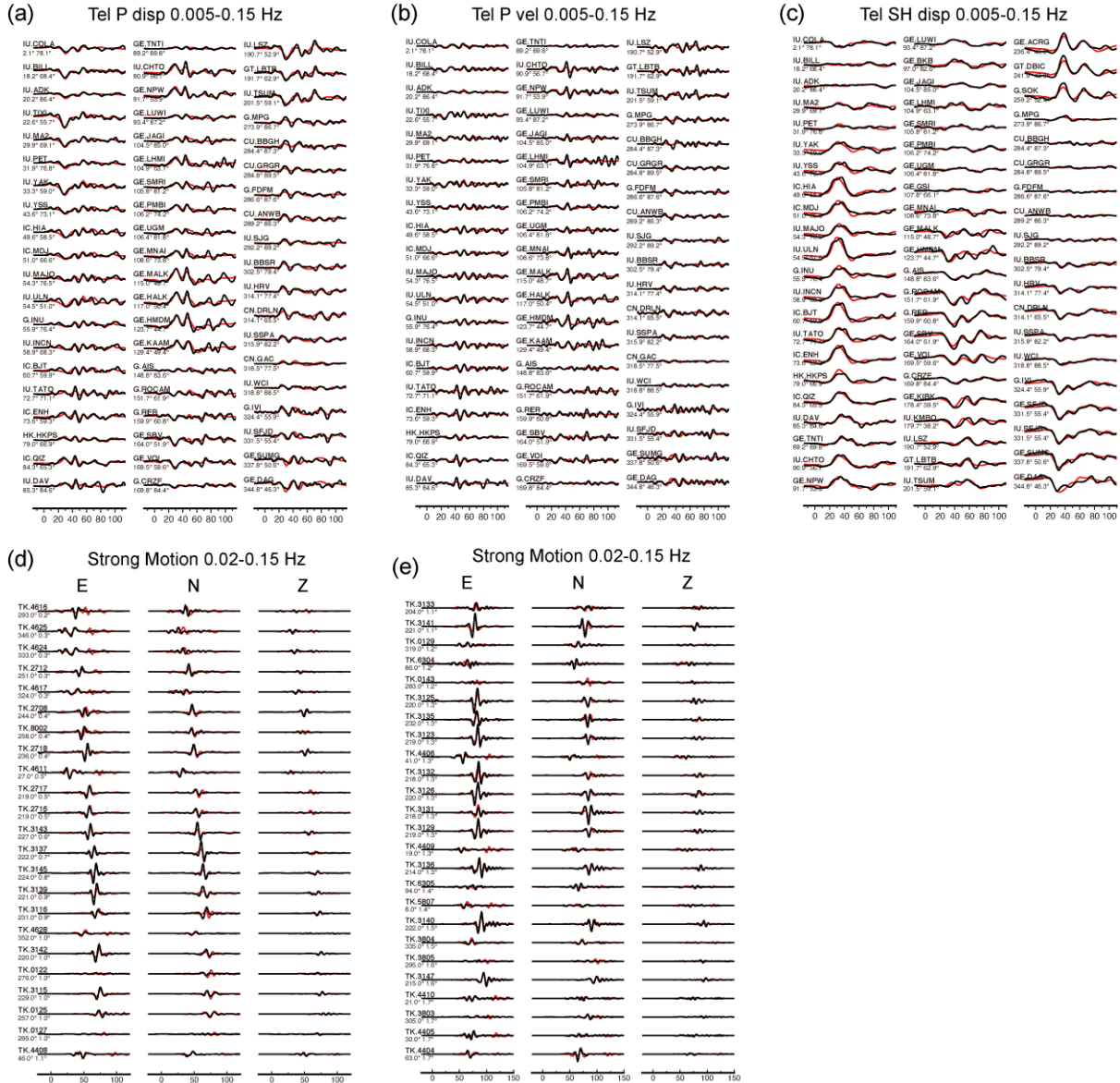


**Fig. S10.**

Waveform fits of the preferred subevent model for the  $M_w$  7.8 event. Observed data and synthetics are indicated by black and red lines, respectively. The numbers leading each trace are the station azimuth and distance. (a) P waves in displacement. (b) P waves in velocity. (c) SH waves in displacement. (d-e) Local full strong motion waveforms in velocity.

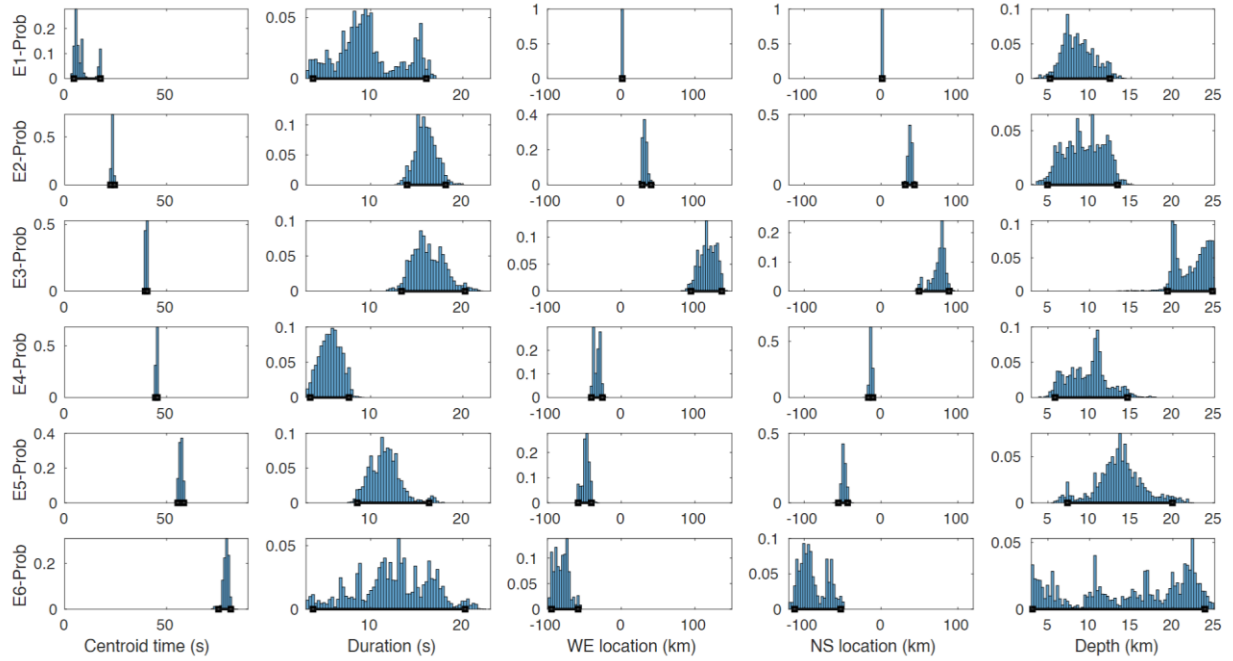


**Fig. S11.**

Subevent model uncertainties from the Markov Chain sample distributions. Columns from left to right indicate the density distribution of subevent centroid times, durations, west-east locations, north-south locations and centroid depths. Rows represent subevents E1-E6.

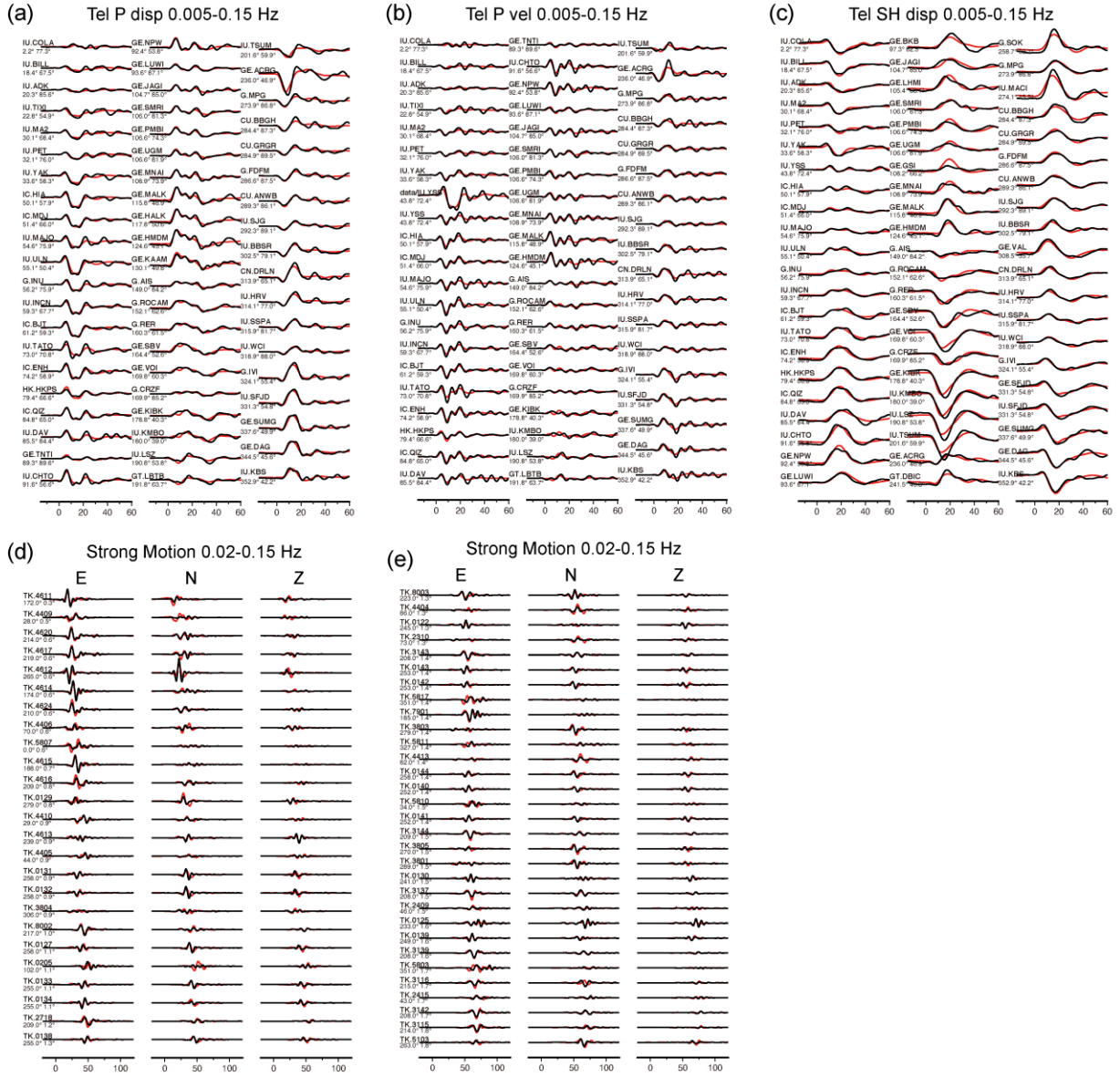


**Fig. S12.**

Similar to Fig. S10 but for the  $M_w$  7.7 event.

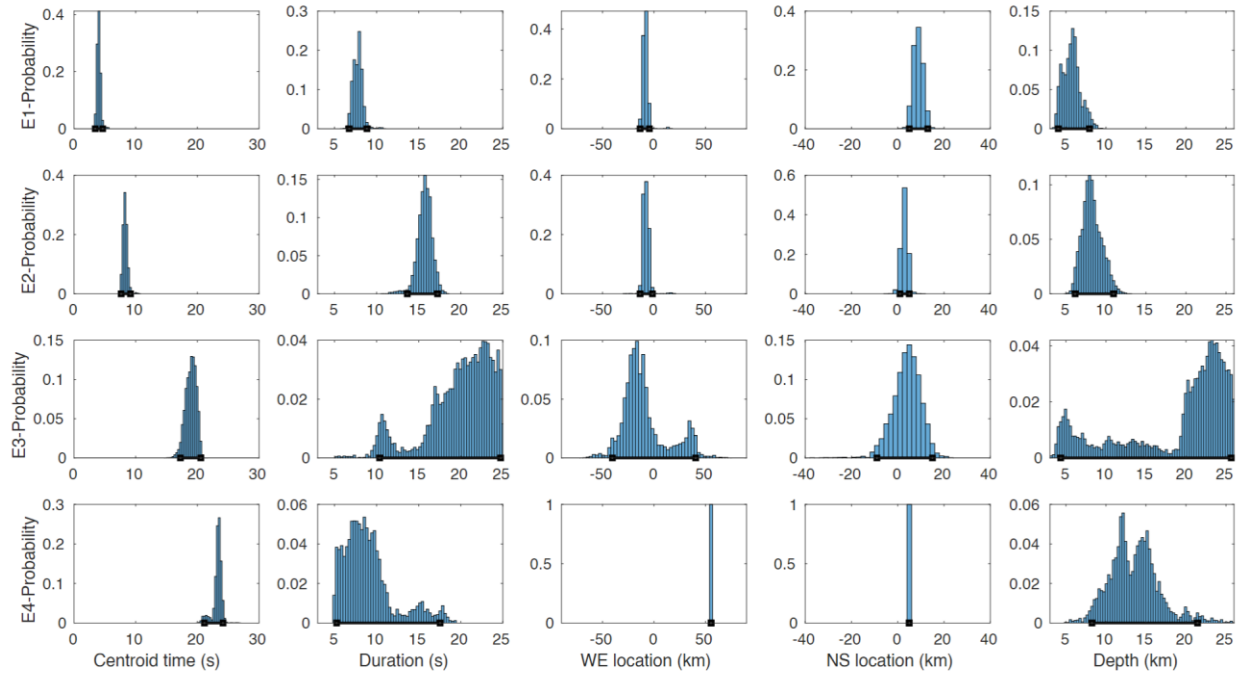


**Fig. S13.**  
 Similar to Fig. S11 but for the  $M_w$  7.7 event.

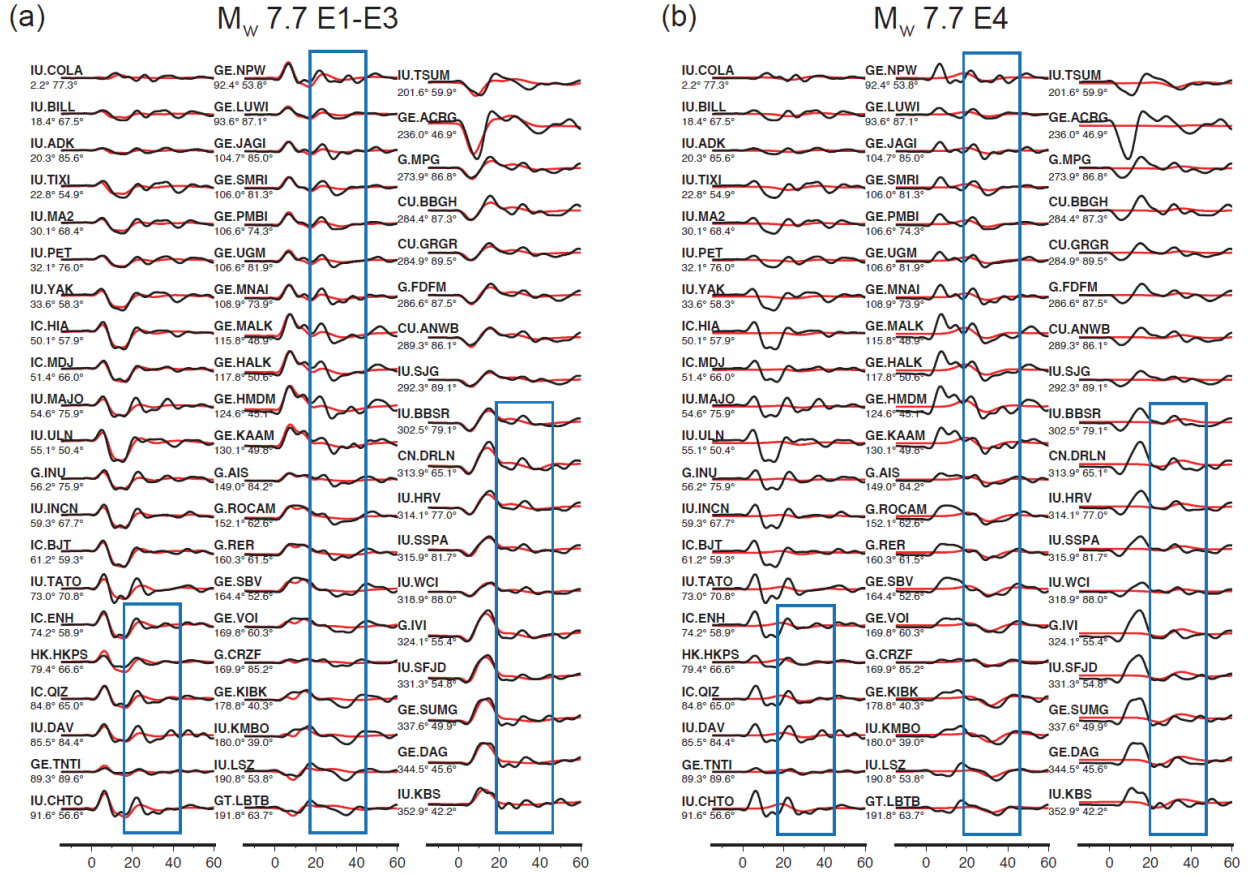


**Fig. S14.**

Contributions to the teleseismic P waves in displacement from (a) subevents E1-E3 and (b) subevent E4 for the  $M_w$  7.7 earthquake. The boxed areas show that the seismic data fits require contribution from E4.

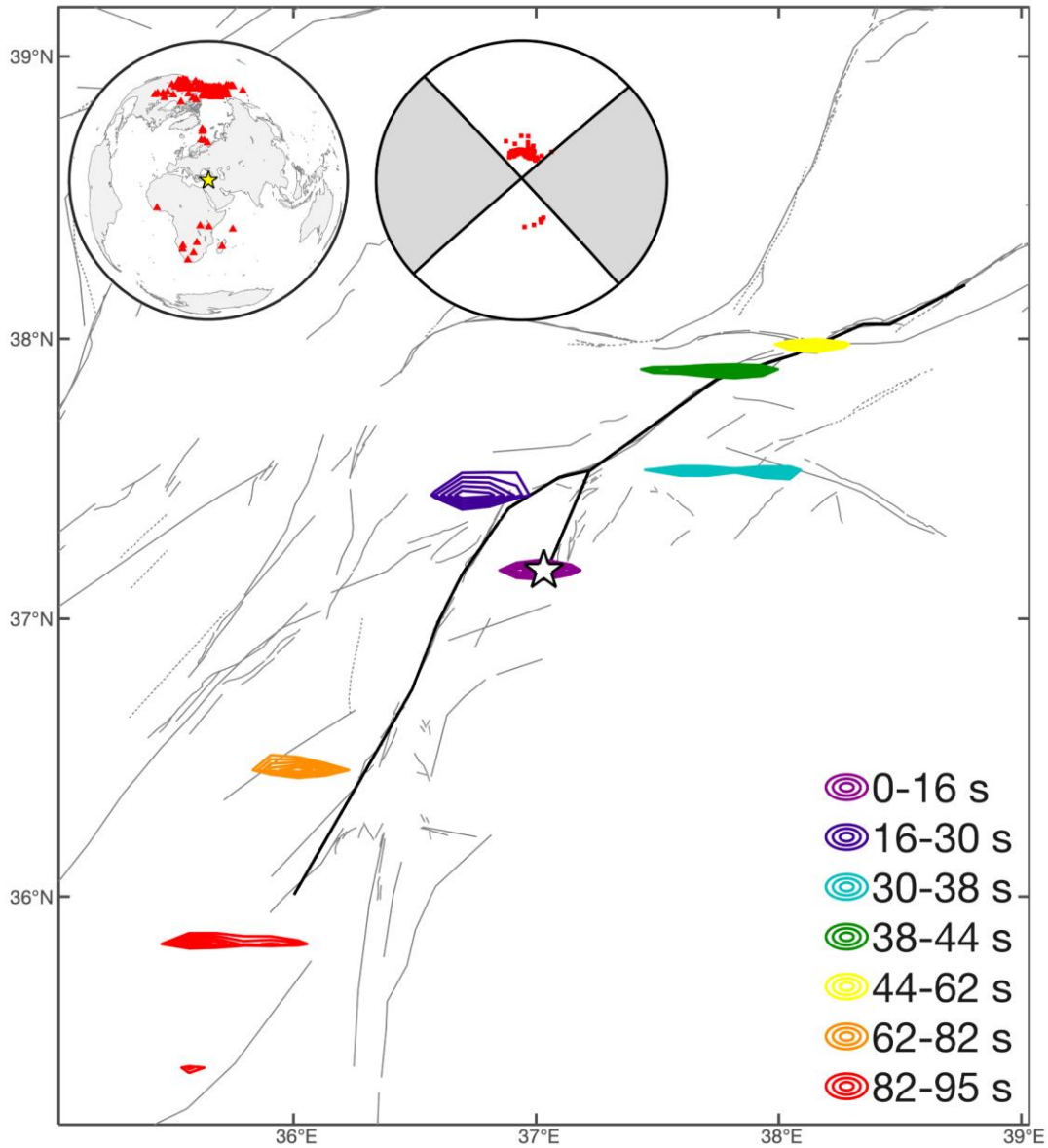


**Fig. S15.**

Back-projection results for the  $M_w$  7.8 earthquake. Color contours indicate the normalized peak energy radiation for specific time windows. Insets display the stations utilized for the analysis and their corresponding P wave polarity in the lower-hemisphere projection.

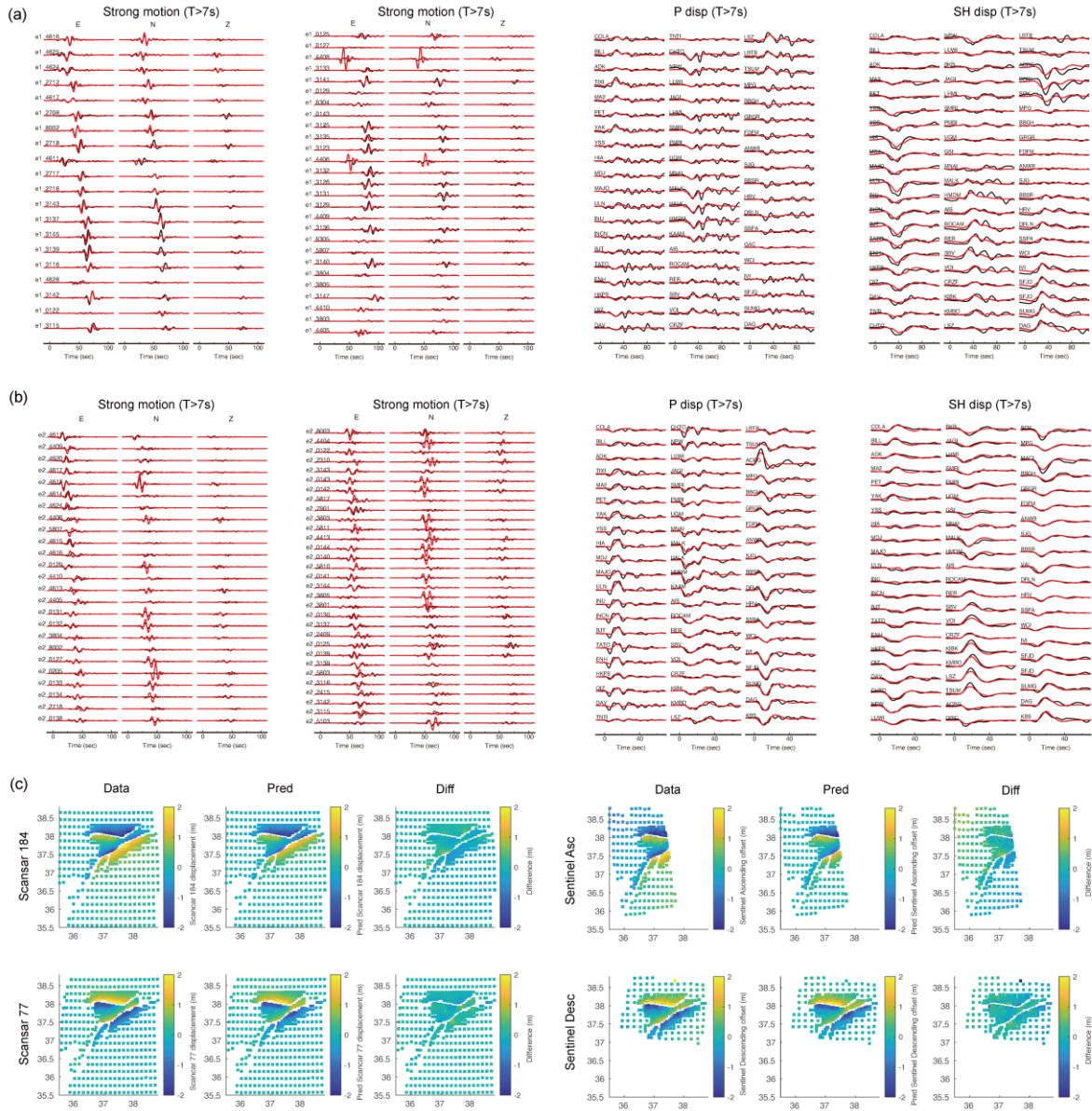


**Fig. S16.**

Data fits of the kinematic finite-fault model. (a) Fits to the near- and far-field seismic waveforms for the  $M_w$  7.8 earthquake. (b) same as (a) but for the  $M_w$  7.7 event. (c) Comparison of data and predictions of line-of-sight displacements for the ScanSAR track 184 and 77, and range offsets for the Sentinel ascending and descending tracks.

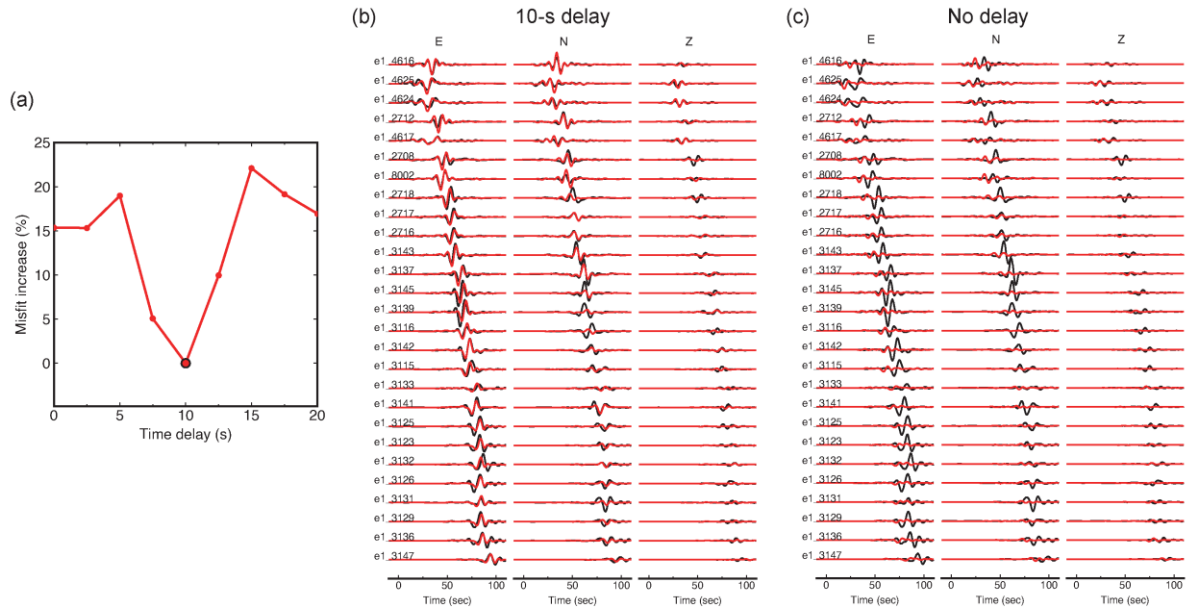


**Fig. S17.**

Delay of the backward branching along the southwest segment of the EAF during the  $M_w$  7.8 earthquake. (a) Optimal delay of 10 s constrained by grid-search. (b) Fits to the on-fault strong-motion waves with 10-s time delay. (c) Fits to the on-fault strong motion waves without time delay.

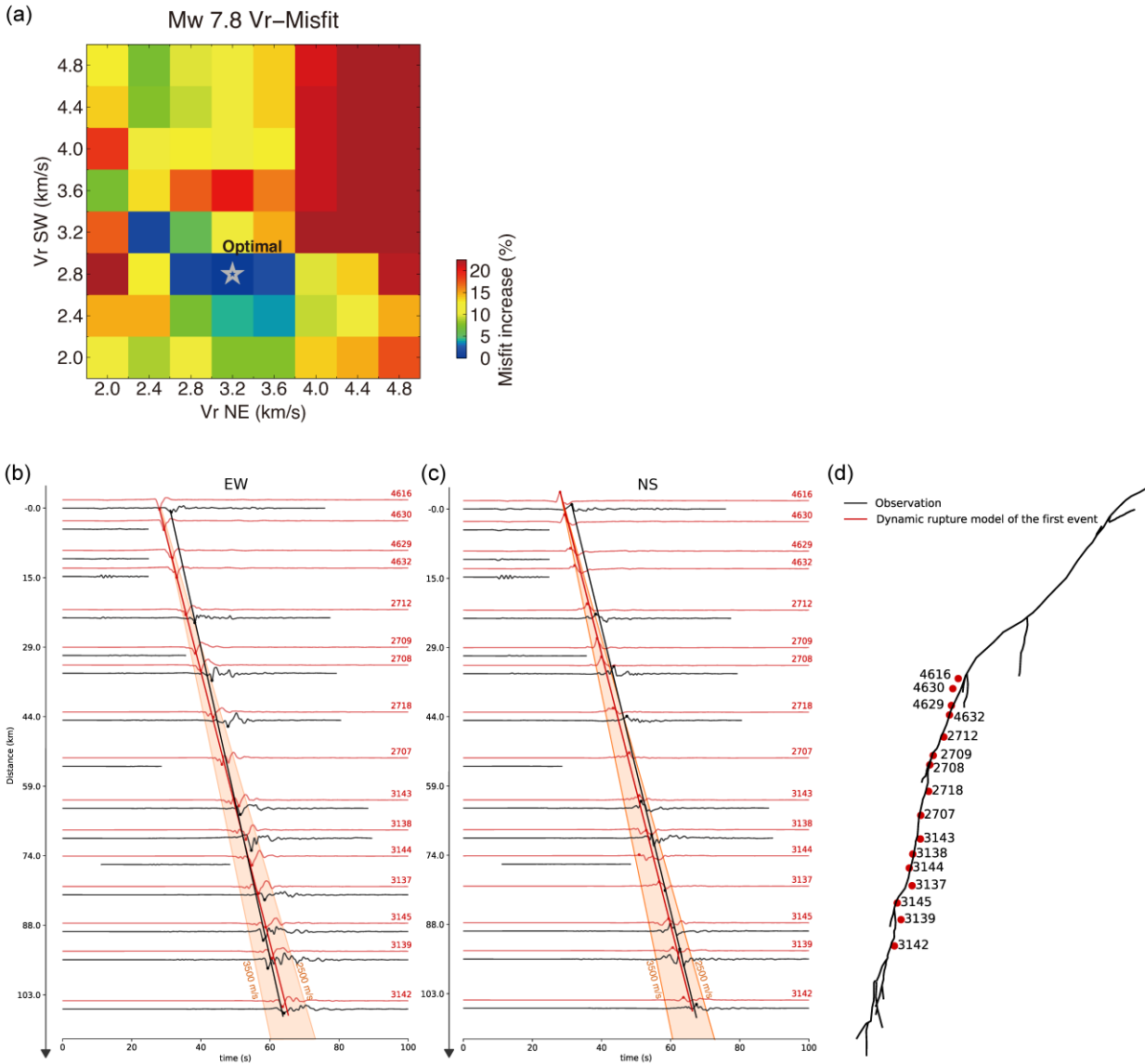


**Fig. S18.**

Rupture velocity analysis for the  $M_w$  7.8 earthquake. (a) Data misfits of the kinematic slip inversion as a function of rupture velocities towards northeast and southwest directions, respectively. (b) Estimates of average rupture speed on the southwestern part of the East Anatolian Fault (EAF), using EW/NS components of the observed (black) and dynamic rupture synthetic (red) ground motions for the stations located atop the SW-EAF. For each station, the observed and modeled ground motions are offset for visibility. We use the respective peak of the first strong velocity pulse, marked by black and red points, in each waveform to estimate the rupture speed. The black and red straight lines are the resulting estimated average rupture speeds.

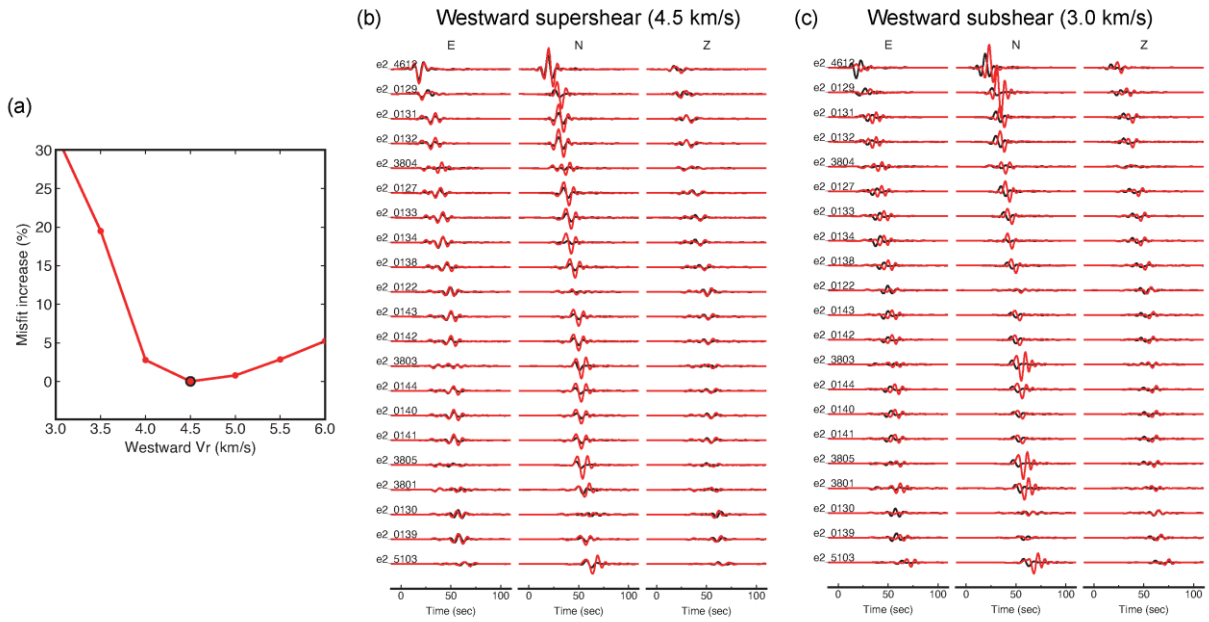


**Fig. S19.**

Westward supershear rupture velocity during the  $M_w$  7.7 earthquake. (a) Optimal westward rupture velocity of 4.5 km/s constrained by grid-search. (b) Fits to the west-propagating strong-motion waves with a supershear rupture velocity of 4.5 km/s. (c) Fits to the west-propagating strong motion waves with a subshear rupture velocity of 3.0 km/s.

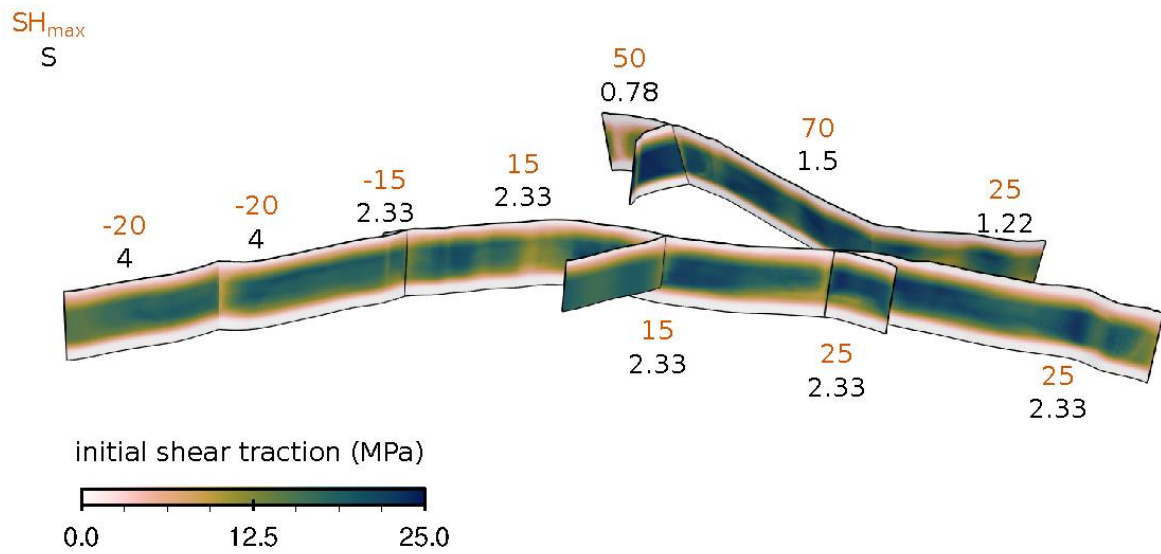


**Fig. S20.**

Initial conditions for dynamic rupture modeling of both large earthquakes.  $SH_{max}$  (orange numbers) is the complex regional maximum horizontal compressional stress loading on all faults and varies across the fault system.  $S$  (black numbers) is the ratio of initial strength excess to nominal stress drop and a measure of the relative strength of each fault segment (85). Additional small-scale initial shear-stress heterogeneity is constrained from the static slip model (Fig. 1).

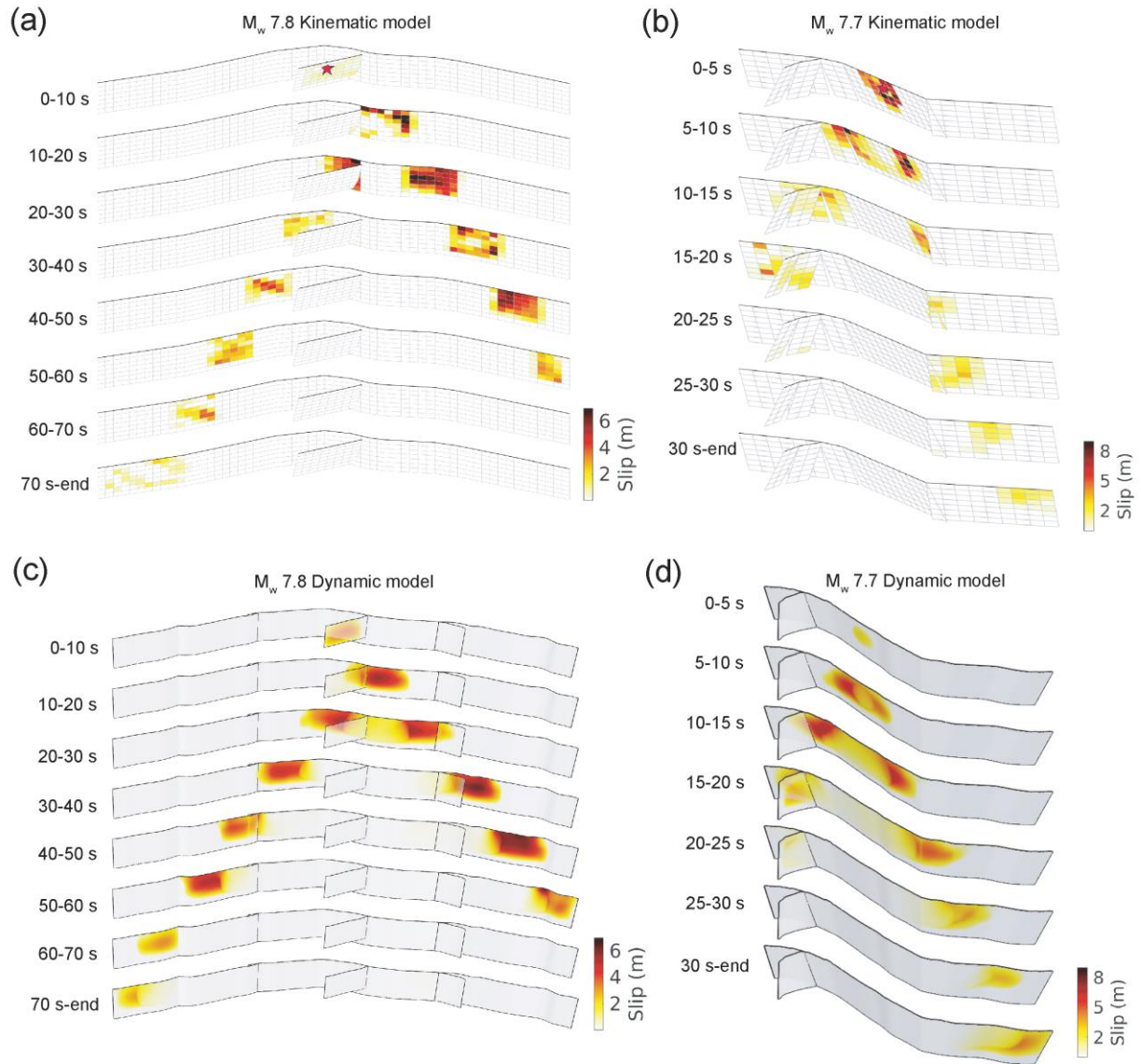


**Fig. S21.**

Comparison of the accumulated slip at different time intervals from kinematic slip models for the (a)  $M_w$  7.8 and (b)  $M_w$  7.7 earthquakes, with dynamic models for the (c)  $M_w$  7.8 and (d)  $M_w$  7.7 earthquakes, respectively.

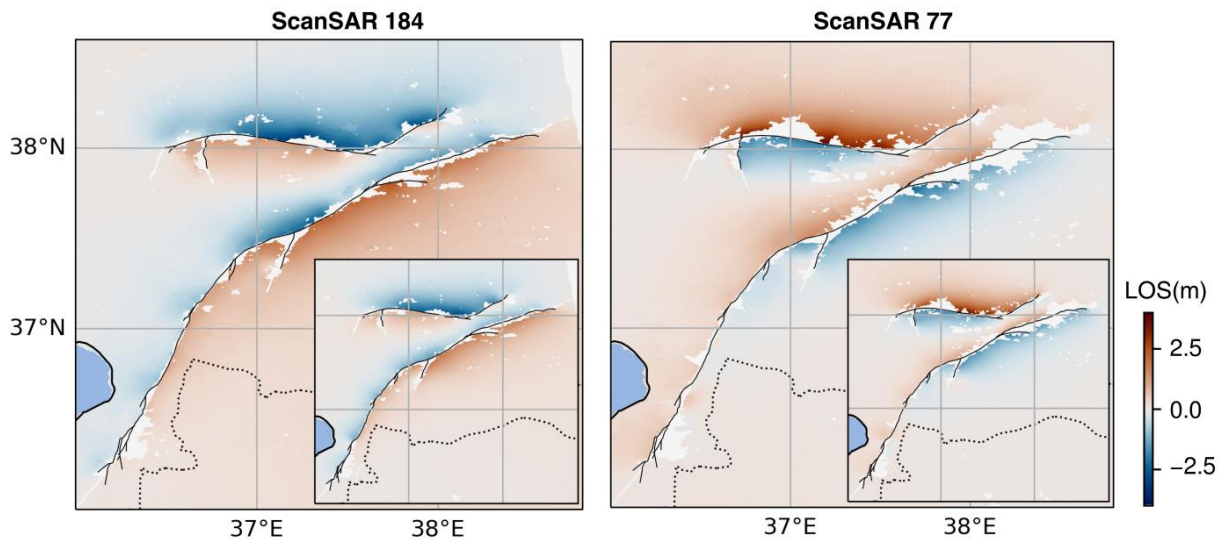


**Fig. S22.**

Comparison of the surface displacements predicted by our dynamic rupture models (inset) with the interferograms derived from ScanSAR data from ALOS-2 ascending track 184 (left) and descending track 77 (right). RMS mismatch between InSAR data and predictions is 0.14 m and 0.12 m for track 184 and 77, respectively.

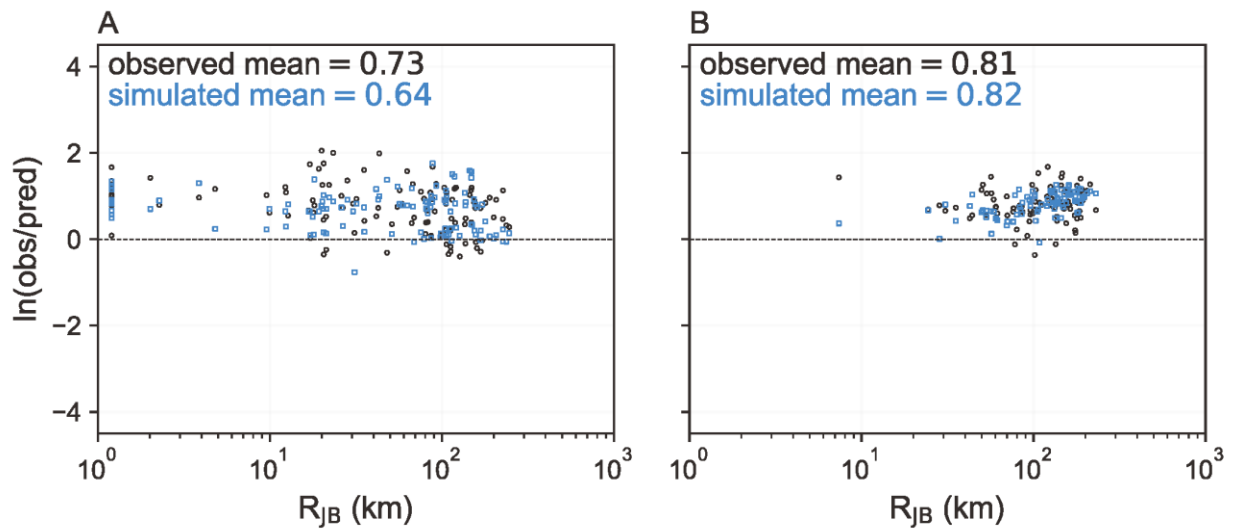


**Fig. S23.**

GMPE (55) residuals for the observed and simulated peak ground velocities (PGV) plotted against Joyner-Boore distance (RJB) for the (a)  $M_w$  7.8 and (b)  $M_w$  7.7 earthquakes of Fig. 5 of the main text. All PGV are rotationally-independent geometric mean values (GMRotD50, 108). The residuals for the observed PGVs are shown by open black circles, and the residuals for the dynamic-rupture-simulated PGVs are shown by open blue squares. We bin the residuals by RJB and indicate the medians for each distance bin with solid markers. The means of the residuals are printed in the upper left of each panel. We include simulated and observed data at the same locations, respectively.

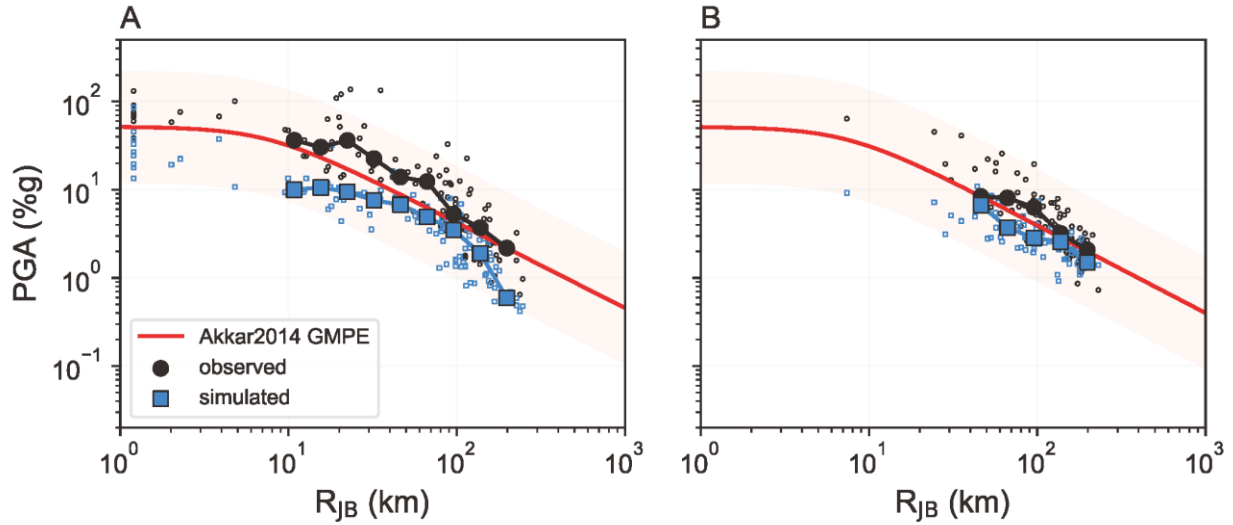


**Fig. S24.**

Similar to Fig. 5 but comparing peak ground accelerations (PGA) plotted against Joyner-Boore distance ( $R_{JB}$ ) for the (a)  $M_w$  7.8 and (b)  $M_w$  7.7 earthquakes. Modeled and observed PGAs, which are more sensitive to high frequency radiation than PGVs, agree to first order. Observed PGAs from strong motion accelerometers are indicated by open black circles, and simulated PGAs from the dynamic rupture simulations are indicated by open blue squares. All PGA are rotationally-independent geometric mean values (GMRotD50). We bin the PGA data and synthetics by  $R_{JB}$  and plot the medians for each distance bin (solid markers). We include simulated and observed data at the same locations, respectively.

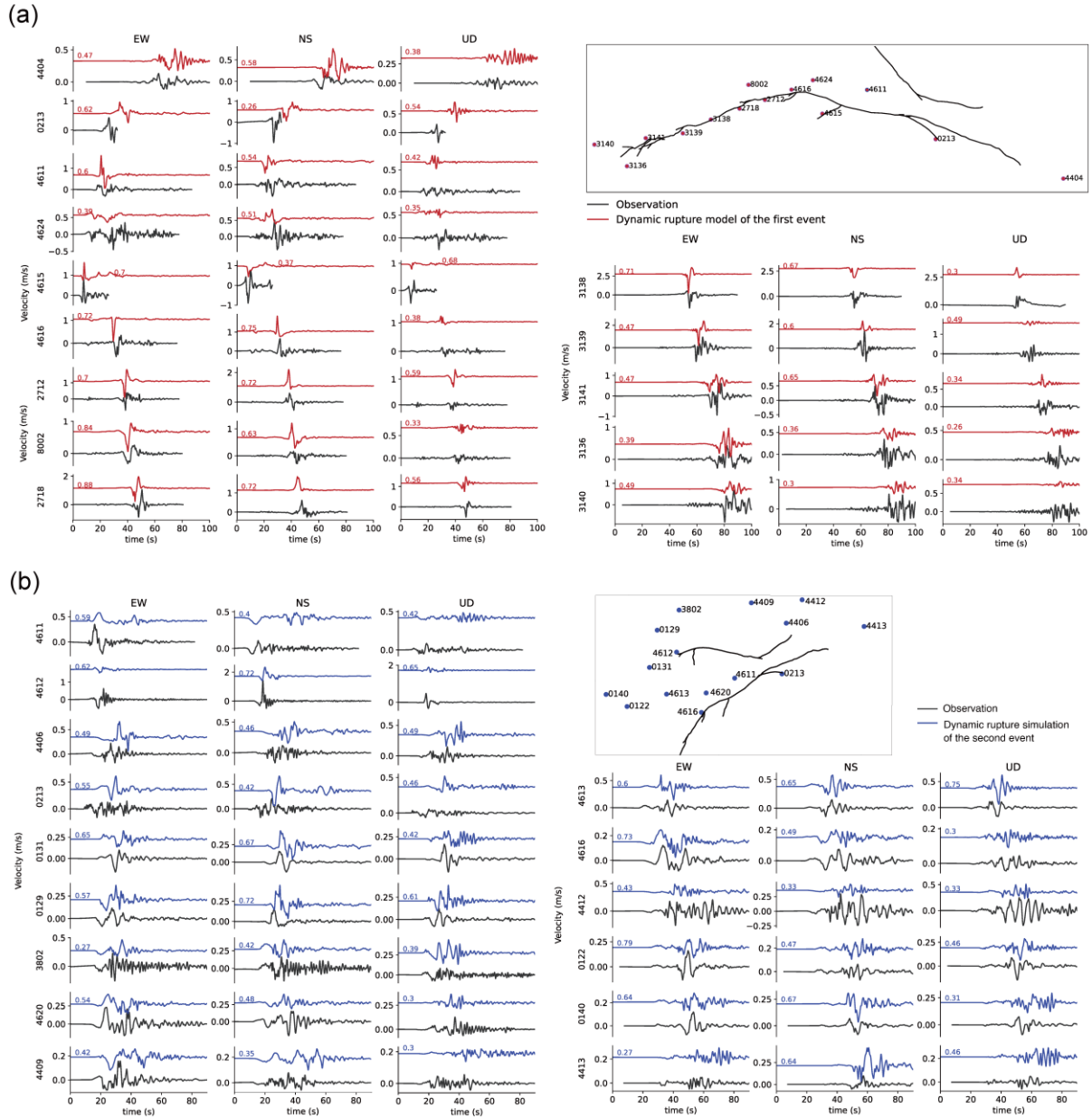


**Fig. S25**

Comparison for the dynamic rupture scenario of modeled (red/blue) and observed strong ground motions (black) for (a) the  $M_w$  7.8 and (b) the  $M_w$  7.7 earthquakes, respectively. Ground velocity time series at near-fault strong-motion stations are band-pass filtered between 0.01-1 Hz. No amplitude scaling or time shifts are applied.

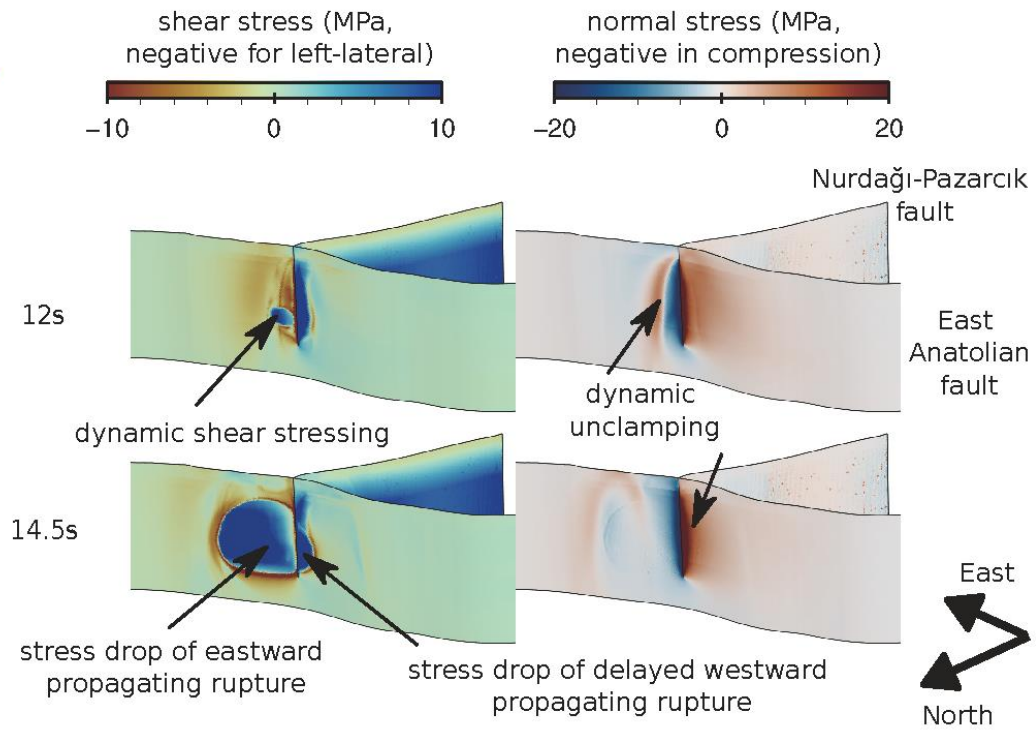


**Fig. S26.**

Transient shear stressing (left) and dynamic unclamping (right) effects at the fault intersection due to the northeastward rupture along the EAF.

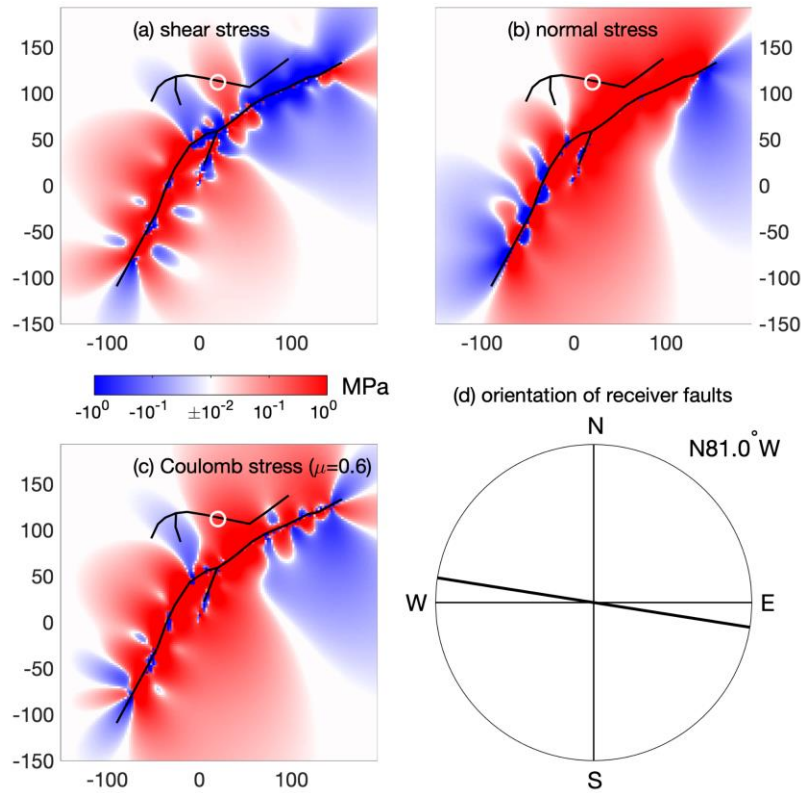


**Fig. S27.**

Static stress changes due to the  $M_w$  7.8 mainshock, resolved on vertical faults striking 279 degrees (81 degrees counterclockwise from north), similar to the strike of the Çardak fault near the nucleation site of the  $M_w$  7.7 event (shown by a white circle). Panels (a), (b), and (c) show the computed perturbations in the shear, normal, and Coulomb stresses, respectively, at the assumed depth of 5 km. Colors represent stress changes, in megapascals, on a logarithmic scale. The calculated Coulomb stress changes assume a coefficient of friction of 0.6. Panel (d) shows the orientation of potential receiver faults. Results for other possible fault orientations are shown in Supplementary Video S3.

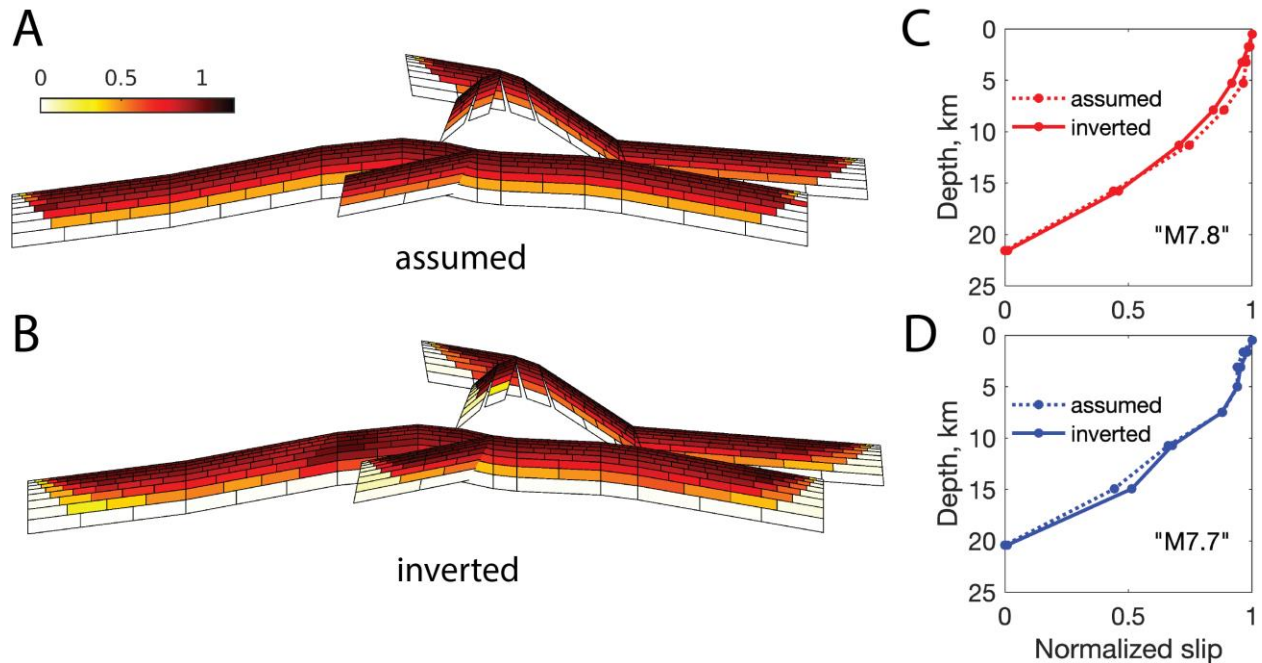


**Fig. S28.**

A synthetic test of the resolving power of our static slip model. We use the preferred fault geometry and assumed slip distribution, as shown in panel (a), to generate synthetic data at the same observation points that were used in our inversions. The resulting data set is then inverted using the same parameters as in inversions of actual data. The resulting slip distribution is shown in panel (b). Panels c and d compare the along-strike averaged normalized slip as a function of depth on faults representing the (c)  $M_w$  7.8 and (d)  $M_w$  7.7 ruptures. Note that the shallow slip is resolved reasonably well, and no apparent deficit is introduced due to some missing near-field data (Fig. S1).

Satellite Mode	Track Number	Preseismic Acquisition Date	Postseismic Acquisition Date
Sentinel-1	Ascending 14	2023/01/28	2023/02/09
Sentinel-1	Ascending 116	2023/02/04	2023/02/28
Sentinel-1	Descending 21	2023/01/29	2023/02/10
ALOS-2 Strip mode	Descending 78	2022/04/06	2023/02/08
ALOS-2 ScanSAR	Ascending 183	2019/09/18	2023/02/15
ALOS-2 ScanSAR	Ascending 184	2022/09/05	2023/02/20
ALOS-2 ScanSAR	Ascending 185	2022/09/10	2023/02/11
ALOS-2 ScanSAR	Descending 76	2022/09/11	2023/02/12
ALOS-2 ScanSAR	Descending 77	2022/09/16	2023/02/17
ALOS-2 ScanSAR	Descending 78	2022/09/07	2023/02/22

**Table S1.**

Coseismic Sentinel-1 and ALOS-2 SAR acquisitions used in this study.

Vp (km/s)	Vs (km/s)	Density (g/cm <sup>3</sup> )	Thickness (km)
3.88	2.04	2.38	1
4.52	2.43	2.46	1
5.62	3.03	2.64	2
5.75	3.31	2.66	2
5.85	3.38	2.68	2
5.96	3.43	2.71	2
6.00	3.44	2.72	2
6.05	3.46	2.73	4
6.32	3.62	2.79	4
6.40	3.67	2.81	5
6.83	3.92	2.92	5
6.89	3.94	2.94	7
7.80	4.40	3.22	8
8.22	4.56	3.37	15
8.30	4.61	3.40	0

**Table S2.**

1D velocity structure used in this study. Model originally from Guvercin et al. (23). The density is derived following the Nafe–Drake empirical relationship (112).

## References and Notes

1. M. Edrik, M. B. D. Tümsa, A. Pinar, E. Altunel, A. C. Zülfikar, “A preliminary report on the February 6, 2023 earthquakes in Türkiye” (Temblor, 2023).
2. T. Lay, L. Ye, Y. Bai, K. F. Cheung, H. Kanamori, The 2018 MW 7.9 Gulf of Alaska earthquake: Multiple fault rupture in the Pacific plate. *Geophys. Res. Lett.* **45**, 9542–9551 (2018).
3. L. Meng, J.-P. Ampuero, J. Stock, Z. Duputel, Y. Luo, V. C. Tsai, Earthquake in a maze: Compressional rupture branching during the 2012  $M_w$  8.6 Sumatra earthquake. *Science* **337**, 724–726 (2012).
4. E. Hauksson, L. M. Jones, K. Hutton, The 1999 M w 7.1 Hector Mine, California, earthquake sequence: Complex conjugate strike-slip faulting. *Bull. Seismol. Soc. Am.* **92**, 1154–1170 (2002).
5. E. Hauksson, L. M. Jones, K. Hutton, D. Eberhart-Phillips, The 1992 Landers earthquake sequence: Seismological observations. *J. Geophys. Res.* **98** (B11), 19835–19858 (1993).
6. Z. E. Ross, B. Idini, Z. Jia, O. L. Stephenson, M. Zhong, X. Wang, Z. Zhan, M. Simons, E. J. Fielding, S.-H. Yun, E. Hauksson, A. W. Moore, Z. Liu, J. Jung, Hierarchical interlocked orthogonal faulting in the 2019 Ridgecrest earthquake sequence. *Science* **366**, 346–351 (2019).
7. A. Ghods, E. Shabaniyan, E. Bergman, M. Faridi, S. Donner, G. Mortezaejad, A. Aziz-Zanjani, The Varzaghan–Ahar, Iran, earthquake doublet (M w 6.4, 6.2): Implications for the geodynamics of northwest Iran. *Geophys. J. Int.* **203**, 522–540 (2015).
8. C. J. Ammon, H. Kanamori, T. Lay, A great earthquake doublet and seismic stress transfer cycle in the central Kuril islands. *Nature* **451**, 561–565 (2008).
9. W. Fan, P. M. Shearer, Local near instantaneously dynamically triggered aftershocks of large earthquakes. *Science* **353**, 1133–1136 (2016).
10. D. D. Oglesby, S. M. Day, Y.-G. Li, J. E. Vidale, The 1999 Hector Mine earthquake: The dynamics of a branched fault system. *Bull. Seismol. Soc. Am.* **93**, 2459–2476 (2003).
11. H. S. Bhat, M. Olives, R. Dmowska, J. R. Rice, Role of fault branches in earthquake rupture dynamics. *J. Geophys. Res.* **112** (B11), B11309 (2007).
12. T. Ulrich, A.-A. Gabriel, J.-P. Ampuero, W. Xu, Dynamic viability of the 2016 Mw 7.8 Kaikōura earthquake cascade on weak crustal faults. *Nat. Commun.* **10**, 1213 (2019).
13. R. Douilly, H. Aochi, E. Calais, A. Freed, Three-dimensional dynamic rupture simulations across interacting faults: The Mw7. 0, 2010, Haiti earthquake. *J. Geophys. Res. Solid Earth* **120**, 1108–1128 (2015).
14. S. Minson, M. Simons, J. Beck, Bayesian inversion for finite fault earthquake source models I—Theory and algorithm. *Geophys. J. Int.* **194**, 1701–1726 (2013).
15. K. Wang, D. S. Dreger, E. Tinti, R. Bürgmann, T. Taira, Rupture process of the 2019 Ridgecrest, California  $M_w$  6.4 foreshock and  $M_w$  7.1 earthquake constrained by seismic and geodetic data. *Bull. Seismol. Soc. Am.* **110**, 1603–1626 (2020).

16. S. Barbot, H. Luo, T. Wang, Y. Hamiel, O. Piatibratova, M. T. Javed, C. Braitenberg, G. Gurbuz, Slip distribution of the February 6, 2023  $M_w$  7.8 and  $M_w$  7.6, Kahramanmaraş, Turkey earthquake sequence in the East Anatolian Fault Zone. *Seismica* 10.26443/seismica.v2i3.502 (2023).
17. D. E. Goldberg, T. Taymaz, N. G. Reitman, A. E. Hatem, S. Yolsal-Çevikbilen, W. D. Barnhart, T. S. Irmak, D. J. Wald, T. Öcalan, W. L. Yeck, B. Özkan, J. A. Thompson Jobe, D. R. Shelly, E. M. Thompson, C. B. DuRoss, P. S. Earle, R. W. Briggs, H. Benz, C. Erman, A. H. Doğan, C. Altuntaş, Rapid characterization of the February 2023 Kahramanmaraş, Türkiye, earthquake sequence. *Seismic Record* **3**, 156–167 (2023).
18. V. Karabacak, Ç. Özkaymak, H. Sözbilir, O. Tatar, B. Aktuğ, Ö. C. Özdağ, R. Çakir, E. Aksoy, F. Koçbulut, M. Softa, E. Akgün, A. Demir, G. Arslan, The 2023 Pazarcık (Kahramanmaraş, Türkiye) earthquake ( $M_w$  7.7): Implications for surface rupture dynamics along the East Anatolian Fault Zone. *J. Geol. Soc. London* **180**, jgs2023–jgs2020 (2023).
19. P. M. Mai, T. Aspiotis, T. A. Aquib, E. V. Cano, D. Castro-Cruz, A. Espindola-Carmona, B. Li, X. Li, J. Liu, R. Matrau, A. Nobile, K. H. Palgunadi, M. Ribot, L. Parisi, C. Suhendi, Y. Tang, B. Yalcin, U. Avşar, Y. Klinger, S. Jónsson, The destructive earthquake doublet of 6 February 2023 in south-central Türkiye and Northwestern Syria: Initial observations and analyses. *Seismic Record* **3**, 105–115 (2023).
20. D. Melgar, T. Taymaz, A. Ganas, B. Crowell, T. Öcalan, M. Kahraman, V. Tsironi, S. Yolsal-Çevikbilen, S. Valkaniotis, T. S. Irmak, T. Eken, C. Erman, B. Özkan, A. H. Dogan, C. Altuntaş, Sub- and super-shear ruptures during the 2023  $M_w$  7.8 and  $M_w$  7.6 earthquake doublet in SE Türkiye. *Seismica* 10.26443/seismica.v2i3.387 (2023).
21. R. Okuwaki, Y. Yagi, T. Taymaz, S. P. Hicks, multi-scale rupture growth with alternating directions in a complex fault network during the 2023 south-eastern Türkiye and Syria earthquake doublet. *Geophys. Res. Lett.* **50**, e2023GL103480 (2023).
22. N. Lyberis, T. Yurur, J. Chorowicz, E. Kasapoglu, N. Gundogdu, The East Anatolian Fault: An oblique collisional belt. *Tectonophysics* **204**, 1–15 (1992).
23. S. E. Güvercin, H. Karabulut, A. Ö. Konca, U. Doğan, S. Ergintav, Active seismotectonics of the East Anatolian Fault. *Geophys. J. Int.* **230**, 50–69 (2022).
24. T. Y. Duman, Ö. Emre, The East Anatolian Fault: Geometry, segmentation and jog characteristics. *Spec. Publ. Geol. Soc. Lond.* **372**, 495–529 (2013).
25. A. Koç, N. Kaymakcı, Kinematics of Sürgü fault zone (Malatya, Turkey): A remote sensing study. *J. Geodyn.* **65**, 292–307 (2013).
26. Materials and methods are available as supplementary materials.
27. Z. Jin, Y. Fialko, Finite slip models of the 2019 Ridgecrest earthquake sequence constrained by space geodetic data and aftershock locations. *Bull. Seismol. Soc. Am.* **110**, 1660–1679 (2020).
28. A. Lomax, Precise, NLL-SSST-coherence hypocenter catalog for the 2023  $M_w$  7.8 and  $M_w$  7.6 SE Turkey earthquake sequence. Zenodo (2023); <https://doi.org/10.5281/zenodo.8089273>.

29. A. Dođru, F. Bulut, C. Yaltırak, B. Aktuđ, Slip distribution of the 2020 Elazıđ Earthquake ( $M_w$  6.75) and its influence on earthquake hazard in the Eastern Anatolia. *Geophys. J. Int.* **224**, 389–400 (2021).
30. Z. Jia, Z. Shen, Z. Zhan, C. Li, Z. Peng, M. Gurnis, The 2018 Fiji  $M_w$  8.2 and 7.9 deep earthquakes: One doublet in two slabs. *Earth Planet. Sci. Lett.* **531**, 115997 (2020).
31. Z. Jia, Z. Zhan, H. Kanamori, The 2021 south Sandwich Island  $M_w$  8.2 Earthquake: A slow event sandwiched between regular ruptures. *Geophys. Res. Lett.* **49**, e2021GL097104 (2022).
32. M. Ishii, P. M. Shearer, H. Houston, J. E. Vidale, Extent, duration and speed of the 2004 Sumatra-Andaman earthquake imaged by the Hi-Net array. *Nature* **435**, 933–936 (2005).
33. Z. Jia, X. Wang, Z. Zhan, Multifault models of the 2019 Ridgecrest sequence highlight complementary slip and fault junction instability. *Geophys. Res. Lett.* **47**, e2020GL089802 (2020).
34. G. Ekström, M. Nettles, A. Dziewoński, The global CMT project 2004–2010: Centroid-moment tensors for 13,017 earthquakes. *Phys. Earth Planet. Inter.* **200-201**, 1–9 (2012).
35. C. Liang, J. P. Ampuero, D. Pino Muñoz, The paucity of supershear earthquakes on large faults governed by rate and state friction. *Geophys. Res. Lett.* **49**, e2022GL099749 (2022).
36. E. M. Dunham, Conditions governing the occurrence of supershear ruptures under slip-weakening friction. *J. Geophys. Res. Solid Earth* **112**, JB004717 (2007).
37. E. Tinti, E. Casarotti, T. Ulrich, T. Taufiqurrahman, D. Li, A.-A. Gabriel, Constraining families of dynamic models using geological, geodetic and strong ground motion data: The  $M_w$  6.5, October 30th, 2016, Norcia earthquake, Italy. *Earth Planet. Sci. Lett.* **576**, 117237 (2021).
38. N. Kame, J. R. Rice, R. Dmowska, Effects of prestress state and rupture velocity on dynamic fault branching. *J. Geophys. Res. Solid Earth* **108**, JB002189 (2003).
39. S. Fliss, H. S. Bhat, R. Dmowska, J. R. Rice, Fault branching and rupture directivity. *J. Geophys. Res. Solid Earth* **110**, JB003368 (2005).
40. G. King, J. Nabecaronlek, Role of fault bends in the initiation and termination of earthquake rupture. *Science* **228**, 984–987 (1985).
41. D. Andrews, Mechanics of fault junctions. *J. Geophys. Res.* **94**, 9389–9397 (1989).
42. B. Duan, D. D. Oglesby, Nonuniform prestress from prior earthquakes and the effect on dynamics of branched fault systems. *J. Geophys. Res. Solid Earth* **112**, JB004443 (2007).
43. A. Rosakis, M. Abdelmeguid, A. Elbanna, Evidence of early supershear transition in the  $M_w$  7.8 Kahramanmaraş earthquake from near-field records. arXiv:2302.07214 [physics.geo-ph] (2023).
44. S. S. Nalbant, J. McCloskey, S. Steacy, A. A. Barka, Stress accumulation and increased seismic risk in eastern Turkey. *Earth Planet. Sci. Lett.* **195**, 291–298 (2002).
45. Y. Fialko, Estimation of absolute stress in the hypocentral region of the 2019 Ridgecrest, California, earthquakes. *J. Geophys. Res. Solid Earth* **126**, e2021JB022000 (2021).

46. Z. Cakir, U. Doğan, A. M. Akoğlu, S. Ergintay, S. Özarpacı, A. Özdemir, T. Nozadkhalil, N. Çakir, C. Zabcı, M. H. Erkoç, M. Basmenji, M. Köküm, R. Bilham, Arrest of the  $M_w$  6.8 January 24, 2020 Elaziğ (Turkey) earthquake by shallow fault creep. *Earth Planet. Sci. Lett.* **608**, 118085 (2023).
47. Y. Kaneko, Y. Fialko, D. T. Sandwell, X. Tong, M. Furuya, Interseismic deformation and creep along the central section of the North Anatolian Fault (Turkey): InSAR observations and implications for rate-and-state friction properties. *J. Geophys. Res. Solid Earth* **118**, 316–331 (2013).
48. E. O. Lindsey, Y. Fialko, Geodetic constraints on frictional properties and earthquake hazard in the Imperial Valley, Southern California. *J. Geophys. Res. Solid Earth* **121**, 1097–1113 (2016).
49. Y. Fialko, D. Sandwell, M. Simons, P. Rosen, Three-dimensional deformation caused by the Bam, Iran, earthquake and the origin of shallow slip deficit. *Nature* **435**, 295–299 (2005).
50. Z. Jin, Y. Fialko, Coseismic and early postseismic deformation due to the 2021  $M7.4$  Maduo (China) earthquake. *Geophys. Res. Lett.* **48**, e2021GL095213 (2021).
51. L. Dal Zilio, J.-P. Ampuero, Earthquake doublet in Turkey and Syria. *Commun. Earth Environ.* **4**, 71 (2023).
52. L. Luzi, F. Pacor, G. Lanzano, C. Felicetta, R. Puglia, M. D’Amico, 2016–2017 Central Italy seismic sequence: Strong-motion data analysis and design earthquake selection for seismic microzonation purposes. *Bull. Earthquake Eng.* **18**, 5533–5551 (2020).
53. Disaster and Emergency Management Authority (AFAD) (1973); <https://depem.afad.gov.tr/event-catalog>.
54. T. Taufiqurrahman, A.-A. Gabriel, D. Li, T. Ulrich, B. Li, S. Carena, A. Verdecchia, F. Gallovič, Dynamics, interactions and delays of the 2019 Ridgecrest rupture sequence. *Nature* **618**, 308–315 (2023).
55. S. Akkar, M. A. Sandıkkaya, J. J. Bommer, Empirical ground-motion models for point-and extended-source crustal earthquake scenarios in Europe and the Middle East. *Bull. Earthquake Eng.* **12**, 359–387 (2014).
56. Z. Jia *et al.*, 2023\_Turkey\_doublet\_Data\_Model. Zenodo (2023); <https://doi.org/10.5281/zenodo.8128343>.
57. D. Sandwell, R. Mellors, X. Tong, M. Wei, P. Wessel, *GMTSAR: An InSAR Processing System Based on Generic Mapping Tools* (Scripps Institution of Oceanography, 2011).
58. T. G. Farr, P. A. Rosen, E. Caro, R. Crippen, R. Duren, S. Hensley, M. Kobrick, M. Paller, E. Rodriguez, L. Roth, D. Seal, S. Shaffer, J. Shimada, J. Umland, M. Werner, M. Oskin, D. Burbank, D. Alsdorf, The shuttle radar topography mission. *Rev. Geophys.* **45**, RG2004 (2007).
59. R. M. Goldstein, H. A. Zebker, C. L. Werner, Satellite radar interferometry: Two-dimensional phase unwrapping. *Radio Sci.* **23**, 713–720 (1988).
60. T. A. Herring, T. I. Melbourne, M. H. Murray, M. A. Floyd, W. M. Szeliga, R. W. King, D. A. Phillips, C. M. Puskas, M. Santillan, L. Wang, Plate Boundary Observatory and

- related networks: GPS data analysis methods and geodetic products. *Rev. Geophys.* **54**, 759–808 (2016).
61. J. Böhm, A. Niell, P. Tregoning, H. Schuh, Global Mapping Function (GMF): A new empirical mapping function based on numerical weather model data. *Geophys. Res. Lett.* **33**, L07304 (2006).
  62. F. Lyard, F. Lefevre, T. Letellier, O. Francis, Modelling the global ocean tides: Modern insights from FES2004. *Ocean Dyn.* **56**, 394–415 (2006).
  63. D. D. McCarthy, G. Petit, “IERS conventions (2003)” (International Earth Rotation And Reference Systems Service, 2004).
  64. K. Wang, Y. Fialko, Slip model of the 2015 Mw 7.8 Gorkha (Nepal) earthquake from inversions of ALOS-2 and GPS data. *Geophys. Res. Lett.* **42**, 7452–7458 (2015).
  65. Y. Fialko, Probing the mechanical properties of seismically active crust with space geodesy: Study of the coseismic deformation due to the 1992  $M_w$  7.3 Landers (southern California) earthquake. *J. Geophys. Res. Solid Earth* **109**, JB002756 (2004).
  66. R. Wang, F. L. Martín, F. Roth, Computation of deformation induced by earthquakes in a multi-layered elastic crust—FORTRAN programs EDGRN/EDCMP. *Comput. Geosci.* **29**, 195–207 (2003).
  67. T. Bodin, M. Sambridge, H. Tkalčić, P. Arroucau, K. Gallagher, N. Rawlinson, Transdimensional inversion of receiver functions and surface wave dispersion. *J. Geophys. Res. Solid Earth* **117**, JB008560 (2012).
  68. S. E. Minson, D. S. Dreger, Stable inversions for complete moment tensors. *Geophys. J. Int.* **174**, 585–592 (2008).
  69. B. Kennett, E. Engdahl, Traveltimes for global earthquake location and phase identification. *Geophys. J. Int.* **105**, 429–465 (1991).
  70. M. Kikuchi, H. Kanamori, Inversion of complex body waves—III. *Bull. Seismol. Soc. Am.* **81**, 2335–2350 (1991).
  71. Y. Qian, S. Ni, S. Wei, R. Almeida, H. Zhang, The effects of core-reflected waves on finite fault inversions with teleseismic body wave data. *Geophys. J. Int.* **211**, 936–951 (2017).
  72. L. Zhu, L. A. Rivera, A note on the dynamic and static displacements from a point source in multilayered media. *Geophys. J. Int.* **148**, 619–627 (2002).
  73. W. Fan, P. M. Shearer, Detailed rupture imaging of the 25 April 2015 Nepal earthquake using teleseismic  $P$  waves. *Geophys. Res. Lett.* **42**, 5744–5752 (2015).
  74. E. Nissen, J. Elliott, R. Sloan, T. Craig, G. Funning, A. Hutko, B. Parsons, T. Wright, Limitations of rupture forecasting exposed by instantaneously triggered earthquake doublet. *Nat. Geosci.* **9**, 330–336 (2016).
  75. D. Wang, N. Takeuchi, H. Kawakatsu, J. Mori, Estimating high frequency energy radiation of large earthquakes by image deconvolution back-projection. *Earth Planet. Sci. Lett.* **449**, 155–163 (2016).
  76. S. P. Hicks, R. Okuwaki, A. Steinberg, C. A. Rychert, N. Harmon, R. E. Abercrombie, P. Bogiatzis, D. Schlaphorst, J. Zahradnik, J.-M. Kendall, Y. Yagi, K. Shimizu, H. Sudhaus,

- Back-propagating supershear rupture in the 2016  $M_w$  7.1 Romanche transform fault earthquake. *Nat. Geosci.* **13**, 647–653 (2020).
77. S. Rost, C. Thomas, Array seismology: Methods and applications. *Rev. Geophys.* **40**, 21–27 (2002).
78. Y. Xu, K. D. Koper, O. Sufri, L. Zhu, A. R. Hutko, Rupture imaging of the Mw 7.9 12 May 2008 Wenchuan earthquake from back projection of teleseismic P waves. *Geochem. Geophys. Geosyst.* 10.1029/2008GC002335 (2009).
79. S. H. Hartzell, T. H. Heaton, Rupture history of the 1984 Morgan Hill, California, earthquake from the inversion of strong motion records. *Bull. Seismol. Soc. Am.* **76**, 649–674 (1986).
80. C. Ji, D. J. Wald, D. V. Helmberger, Source description of the 1999 Hector Mine, California, earthquake, part I: Wavelet domain inversion theory and resolution analysis. *Bull. Seismol. Soc. Am.* **92**, 1192–1207 (2002).
81. M. Grant, S. Boyd, CVX: Matlab software for disciplined convex programming, version 2.1 (CVX Research, 2014).
82. R. A. Harris, M. Barall, D. J. Andrews, B. Duan, S. Ma, E. M. Dunham, A.-A. Gabriel, Y. Kaneko, Y. Kase, B. T. Aagaard, D. D. Oglesby, J.-P. Ampuero, T. C. Hanks, N. Abrahamson, Verifying a computational method for predicting extreme ground motion. *Seismol. Res. Lett.* **82**, 638–644 (2011).
83. M. D. Ramos, P. Thakur, Y. Huang, R. A. Harris, K. J. Ryan, Working with dynamic earthquake rupture models: A practical guide. *Seismol. Res. Lett.* **93**, 2096–2110 (2022).
84. D. Andrews, Rupture propagation with finite stress in antiplane strain. *J. Geophys. Res.* **81**, 3575–3582 (1976).
85. S. Das, K. Aki, Fault plane with barriers: A versatile earthquake model. *J. Geophys. Res.* **82**, 5658–5670 (1977).
86. E. H. Madden, T. Ulrich, A. A. Gabriel, The state of pore fluid pressure and 3D megathrust earthquake dynamics. *J. Geophys. Res. Solid Earth* **127**, e2021JB023382 (2022).
87. J. R. Rice, “Fault stress states, pore pressure distributions, and the weakness of the San Andreas fault” in *International geophysics* (Elsevier, 1992), vol. 51, pp. 475–503.
88. J. Suppe, Fluid overpressures and strength of the sedimentary upper crust. *J. Struct. Geol.* **69**, 481–492 (2014).
89. S. Wollherr, A. A. Gabriel, P. M. Mai, Landers 1992 “reloaded”: Integrative dynamic earthquake rupture modeling. *J. Geophys. Res. Solid Earth* **124**, 6666–6702 (2019).
90. T. Ulrich, A.-A. Gabriel, E. H. Madden, Stress, rigidity, and sediment strength control megathrust earthquake and tsunami dynamics. *Nat. Geosci.* **15**, 67–73 (2022).
91. J. R. Weiss, R. J. Walters, Y. Morishita, T. J. Wright, M. Lazecky, H. Wang, E. Hussain, A. J. Hooper, J. R. Elliott, C. Rollins, C. Yu, P. J. González, K. Spaans, Z. Li, B. Parsons, High-resolution surface velocities and strain for Anatolia from Sentinel-1 InSAR and GNSS data. *Geophys. Res. Lett.* **47**, e2020GL087376 (2020).
92. S. Peyrat, K. Olsen, Nonlinear dynamic rupture inversion of the 2000 Western Tottori, Japan, earthquake. *Geophys. Res. Lett.* 10.1029/2003GL019058 (2004).

93. F. Gallovič, L. Valentová, J. P. Ampuero, A. A. Gabriel, Bayesian dynamic finite-fault inversion: 1. Method and synthetic test. *J. Geophys. Res. Solid Earth* **124**, 6949–6969 (2019).
94. E. Tinti, P. Spudich, M. Cocco, Earthquake fracture energy inferred from kinematic rupture models on extended faults. *J. Geophys. Res. Solid Earth* **110**, JB003644 (2005).
95. H. Weng, H. Yang, Constraining frictional properties on fault by dynamic rupture simulations and near-field observations. *J. Geophys. Res. Solid Earth* **123**, 6658–6670 (2018).
96. A. M. Rubin, J. P. Ampuero, Earthquake nucleation on (aging) rate and state faults. *J. Geophys. Res. Solid Earth* **110**, JB003686 (2005).
97. R. A. Harris, M. Barall, B. Aagaard, S. Ma, D. Roten, K. Olsen, B. Duan, D. Liu, B. Luo, K. Bai, J.-P. Ampuero, Y. Kaneko, A.-A. Gabriel, K. Duru, T. Ulrich, S. Wollherr, Z. Shi, E. Dunham, S. Bydlon, Z. Zhang, X. Chen, S. N. Somala, C. Pelties, J. Tago, V. M. Cruz-Atienza, J. Kozdon, E. Daub, K. Aslam, Y. Kase, K. Withers, L. Dalguer, A suite of exercises for verifying dynamic earthquake rupture codes. *Seismol. Res. Lett.* **89**, 1146–1162 (2018).
98. S. Wollherr, A.-A. Gabriel, C. Uphoff, Off-fault plasticity in three-dimensional dynamic rupture simulations using a modal Discontinuous Galerkin method on unstructured meshes: Implementation, verification and application. *Geophys. J. Int.* **214**, 1556–1584 (2018).
99. D. Roten, K. Olsen, S. Day, Y. Cui, D. Fäh, Expected seismic shaking in Los Angeles reduced by San Andreas fault zone plasticity. *Geophys. Res. Lett.* **41**, 2769–2777 (2014).
100. M. Dumbser, M. Käser, An arbitrary high-order discontinuous Galerkin method for elastic waves on unstructured meshes—II. The three-dimensional isotropic case. *Geophys. J. Int.* **167**, 319–336 (2006).
101. A. Heinecke, A. Breuer, S. Rettenberger, M. Bader, A.-A. Gabriel, C. Pelties, A. Bode, W. Barth, X.-K. Liao, K. Vaidyanathan, in *SC'14: Proceedings of the International Conference for High Performance Computing, Networking, Storage and Analysis* (IEEE, 2014), pp. 3–14.
102. S. Rettenberger, O. Meister, M. Bader, A.-A. Gabriel, in *Proceedings of the Exascale Applications and Software Conference 2016* (2016), pp. 1–9.
103. C. Uphoff, S. Rettenberger, M. Bader, E. H. Madden, T. Ulrich, S. Wollherr, A.-A. Gabriel, in *Proceedings of the International Conference for High Performance Computing, Networking, Storage and Analysis* (2017), pp. 1–16.
104. C. Pelties, A.-A. Gabriel, J.-P. Ampuero, Verification of an ADER-DG method for complex dynamic rupture problems. *Geosci. Model Dev.* **7**, 847–866 (2014).
105. D. Andrews, Rupture models with dynamically determined breakdown displacement. *Bull. Seismol. Soc. Am.* **94**, 769–775 (2004).
106. Y. A. Fialko, A. M. Rubin, What controls the along-strike slopes of volcanic rift zones? *J. Geophys. Res.* **104** (B9), 20007–20020 (1999).

107. L. L. Erickson, “A three-dimensional dislocation program with applications to faulting in the earth”, thesis, Stanford University (1986).
108. D. M. Boore, J. Watson-Lamprey, N. A. Abrahamson, Orientation-independent measures of ground motion. *Bull. Seismol. Soc. Am.* **96** (4A), 1502–1511 (2006).
109. W. B. Joyner, D. M. Boore, Peak horizontal acceleration and velocity from strong-motion records including records from the 1979 Imperial Valley, California, earthquake. *Bull. Seismol. Soc. Am.* **71**, 2011–2038 (1981).
110. D. J. Wald, B. C. Worden, V. Quitoriano, K. L. Pankow, “ShakeMap manual: technical manual, user’s guide, and software guide” (2005).
111. M. Pagani, D. Monelli, G. Weatherill, L. Danciu, H. Crowley, V. Silva, P. Henshaw, L. Butler, M. Nastasi, L. Panzeri, M. Simionato, D. Vigano, OpenQuake engine: An open hazard (and risk) software for the global earthquake model. *Seismol. Res. Lett.* **85**, 692–702 (2014).
112. T. M. Brocher, Empirical relations between elastic wavespeeds and density in the Earth’s crust. *Bull. Seismol. Soc. Am.* **95**, 2081–2092 (2005).